Review

Edvinas Skliutas, Migle Lebedevaite, Elmina Kabouraki, Tommaso Baldacchini,
Jolita Ostrauskaite, Maria Vamvakaki, Maria Farsari, Saulius Juodkazis and
Mangirdas Malinauskas*

Polymerization mechanisms initiated by spatio-temporally confined light

Abstract: Ultrafast laser 3D lithography based on non-linear light–matter interactions, widely known as multi-photon lithography (MPL), offers unrivaled precision rapid prototyping and flexible additive manufacturing options. 3D printing equipment based on MPL is already commercially available, yet there is still no comprehensive understanding of factors determining spatial resolution, accuracy, fabrication throughput, repeatability, and standardized metrology methods for the accurate characterization of the produced 3D objects and their functionalities. The photoexcitation mechanisms, spatial-control or photo-modified volumes, and the variety of processable materials are topics actively investigated. The complexity of the research field is underlined by a limited understanding and fragmented knowledge of light-excitation and material response. Research to date has only provided case-specific findings on photoexcitation, chemical modification, and material characterization of the experimental data. In this review, we aim to provide a consistent and comprehensive summary of the existing literature on photopolymerization mechanisms under highly confined spatial and temporal conditions, where, besides the excitation and cross-linking, parameters such as diffusion, temperature accumulation, and the finite amount of monomer molecules start to become of critical importance. Key parameters such as photoexcitation, polymerization kinetics, and the properties of the additively manufactured materials at the nanoscale in 3D are examined, whereas, the perspectives for future research and as well as emerging applications are outlined.

Keywords: 3D printing; light-matter interaction; material engineering; multi-photon lithography; nanoscale; photopolymerization.

*Corresponding author: Mangirdas Malinauskas, Laser Research Center, Physics Faculty, Vilnius University, Sauletekio Ave. 10, Vilnius, Lithuania; and World Research Hub Initiative (WRHI), School of Materials and Chemical Technology, Tokyo Institute of Technology, 2-12-1, Ookayama, Meguro-ku, Tokyo 152-8550, Japan,
E-mail: mangirdas.malinauskas@ff.vu.lt. https://orcid.org/0000-0002-6937-4284
Edvinas Skliutas, Laser Research Center, Physics Faculty, Vilnius University, Sauletekio Ave. 10, Vilnius, Lithuania,
E-mail: edvinas.skliutas@ff.vu.lt. https://orcid.org/0000-0001-5226-2801
Migle Lebedevaite and Jolita Ostrauskaite, Department of Polymer Chemistry and Technology, Kaunas University of Technology, Radvilenu Rd. 19, LT-50254 Kaunas, Lithuania,
E-mail: migle.lebedevaite@ktu.lt (M. Lebedevaite), jolita.ostrauskaite@ktu.lt (J. Ostrauskaite). https://orcid.org/0000-0001-8600-7040 (J. Ostrauskaite)
Elmina Kabouraki and Maria Farsari, Institute of Electronic Structure and Laser, Foundation for Research and Technology-Hellas (FORTH-IESL), 70013 Heraklion, Greece, E-mail: elmina@iesl.forth.gr (E. Kabouraki), mfarsari@iesl.forth.gr (M. Farsari). https://orcid.org/0000-0003-2435-4156 (M. Farsari)
Tommaso Baldacchini, Department of Chemistry, University of California, Irvine, CA 92697, USA, E-mail: tbaldacc@uci.edu. https://orcid.org/0000-0001-9246-1653
Maria Vamvakaki, Department of Materials Science and Technology, University of Crete, 70013 Heraklion, Greece,
E-mail: vamvakak@iesl.forth.gr. https://orcid.org/0000-0003-2150-9415
Saulius Juodkazis, Optical Sciences Centre and ARC Training Centre in Surface Engineering for Advanced Materials (SEAM), School of Science, Swinburne University of Technology, Hawthorn, VIC 3122, Australia; and World Research Hub Initiative (WRHI), School of Materials and Chemical Technology, Tokyo Institute of Technology, 2-12-1, Ookayama, Meguro-ku, Tokyo 152-8550, Japan,
E-mail: sjuodkazis@swin.edu.au. https://orcid.org/0000-0003-3542-3874

Acronyms, symbols, parameters, typical values (see Tables 1 and 2).

1 Introduction: state-of-the-art and rising demands

Light is an attractive energy source for science and industry, as it can be used to produce controlled interactions

Table 1: Acronyms and symbols most commonly used in the text.

Acronym	Description	Acronym	Description
1PA	One-photon absorption	2PA	Two-photon absorption
MPA	Multi-photon absorption	MPI	Multi-photon ionization
AI	Avalanche ionization	TI	Tunnel ionization
2PP	Two-photon polymerization	MPL	Multi-photon lithography
LDW	Laser direct write	PI	Photoinitiator
I	Light intensity	I_{pt}, I_{dt}	Light intensity threshold, required to induce polymerization and optical damage
ν	Scanning velocity	λ	Light wavelength
τ	Pulse duration	R	Pulse repetition rate
E_p	Pulse energy	P_a, P_p	Average/peak power
D	Accumulated energy dose	F, F_v	Energy fluence per area/volume. If index p appears, it marks fluence per single pulse
W_{abs}	Energy density absorbed by the material per single pulse	d_r, l_z	Lateral and longitudinal voxel dimensions
NA	Numerical aperture	$\tilde{n}$	Refractive index
R^*	Free-radical	RM^*	Monomeric radical
K^+/A^-	Cation/anion	KM^+X^-/AM^-X^+	Macrocation/macroanion
DC	Degree of conversion	DFW	Dynamic fabrication window
STED	Stimulated-emission depletion microscopy	SLM	Spatial light modulator
DMD	Digital micromirror device	DOE	Diffractive optical element

Table 2: Studied parameters and their typical used values [1].

Parameter	Value	Comments and supporting references
λ	515, 800 and 1030 nm	400, 532 and 1064 nm are also possible [2–4]
τ	10–325 fs	ps, ns and CW are also possible [5–7]
R	1 kHz–100 MHz	Single pulse [8, 9] and GHz [10] reported, too
ν	100 µm/s (10–10,000 µm/s)	Not relevant for projection/interference lithography
t_{exp}	10 µs–10 ms	0.1–10 s exposure can be applied in interference lithography [11]
P_a	0.02–70 mW	More than 100 mW power can be applied in interference lithography [12]
P_p	0.3–47 kW	Peak power per pulse is more important than the average [13]
E_p	0.1–7 nJ	Lower than 0.1 nJ [14] and higher than 7 nJ [15] values can be observed
D	20 pJ–650 µJ	Accumulated dose of multiple individual pulses
NA	1.4 (1.35–1.45)	Only tight focusing or immersion oil objectives ($NA > 1.3$) are considered [16].
F [a]	3 µJ/cm^2–21 kJ/cm^2	Accumulated exposure dose per area at the sample
I [a]	0.2–7 TW/cm^2	>20 TW/cm^2 can be calculated, if assuming 100% objective transmittance
I_v [a]	2–150 TW/cm^3	Towards considering the energy is absorbed within volume not at the surface
W_{abs} [b]	80 pJ/cm^3–0.3 mJ/cm^3	Absorbed energy density per single pulse

[a] Major calculations were performed for $R = 0.2$ MHz, $\tau = 300$ fs and $\lambda = 515$ nm parameters, taking into account transmittance of 26% for $NA = 1.4$ objective, found in the literature [17]. It was assessed, that altering irradiation and writing parameters while remaining objective transmittance constant, calculated F, I and I_v values were allocated in the provided range, as depicted in the Table 2. [b] W_{abs} was calculated using I_v values for single pulse of 300 fs duration and primary electrons density of 10^{10} cm^{-3} [18].

in a large variety of materials. Coherent laser irradiation is useful as it can focus down to fine dimensions and, being monochromatic, induce well-defined interactions required for spectroscopy, microscopy, and material processing. Cell phones can deliver light to CMOS pixels of tens of micrometers and standard microscope objectives can focus light into its wavelength. Furthermore, current electronic devices are operating with mass-produced, sub-10 nm feature chips, made using deep-UV sources. Since becoming more reliable and robust, ultrashort-pulse lasers have evolved into a common tool for precision 3D micro-/nano-fabrication, as high bursts of energy can be delivered in femtoseconds, allowing the induction and observation of reactions in this time range. Nowadays, both spatial and
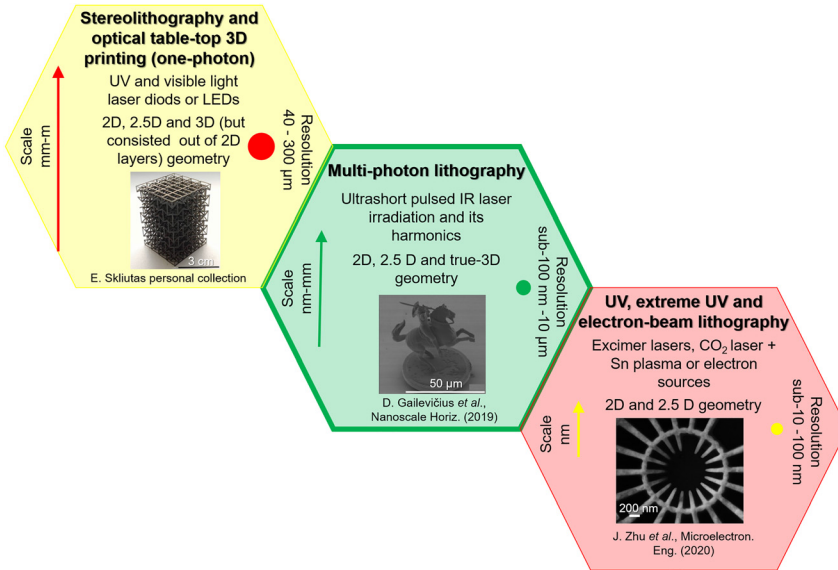
Figure 1: Types of lithography and its capabilities. Pictures reprinted with permission from [20] and [21].

temporal concentration of light is routinely employed in modern optical laboratories. It is used for diverse material and structure modification including material processing and rapid prototyping. Ultrafast laser 3D lithography based on non-linear light–matter interaction became known as two-photon polymerization (2PP, TPP, or multi-photon lithography (MPL)). Now it is a well-established technological field (as shown in Figure 1). As a laser direct writing (LDW) tool it offers unrivalled precision and flexibility in additive manufacturing. 3D printing equipment based on MPL is already commercially available, yet there is still no in-depth understanding of factors determining spatial resolution, accuracy, fabrication throughput, repeatability, and standardized metrology methods for the accurate characterization of the produced 3D objects and their functionalities. The photoexcitation mechanisms, spatial-control or photo-modified volumes, and the variety of efficiently processable materials are still researched topics [19]. The complexity of the research field is underlined by the limited current understanding and the highly fragmented knowledge of light-excitation, material response, and the resulting 3D structure function within the spatio-temporal scale.

In this review, we aim to provide a consistent and comprehensive summary of the existing literature on photopolymerization mechanisms under highly confined spatial and temporal conditions, where, besides the excitation and cross-linking, parameters such as diffusion, temperature accumulation, and the finite amount of monomer molecules start to become game of critical importance. The key parameters, photoexcitation, polymerization kinetics and the properties of the additively manufactured materials at the nanoscale in 3D are

examined, whereas, the perspectives for future research and as well as emerging applications are outlined. We survey the current state of MPL, its advances and identify voids. We provide a detailed interpretation of light matter-interaction mechanisms based on the latest findings, its peculiarities, and influence for material cross-linking. A comparison to single-photon absorption (1PA using UV wavelength) initiated 3D lithography is given where applies (temperature accumulation, monomer diffusion, etc.) based on reported relevant data. Intensity thresholds determining the formation of 3D objects are discussed, and advances in approaches for the modulation of the excitation beams are illustrated. Furthermore, some **case studies** are presented, to stress certain details of experimental or theoretical works of MPL and main findings or results of it. This is important for a newcomer and experienced researcher or engineer working in the field to go fast forward to **TPP** – (*Towards Perfect Polymerization*).

2 Light–matter interaction mechanisms

Light–matter interaction mechanisms can vary, depending on applied intensity, exposure duration, light wavelength and polarization, and material properties. Let's consider some general examples. If the intensity is very low, up to 10^3 W/cm^2, only heating is observed. Increasing the intensity up to 10^3–10^5 W/cm^2, melting of the sample surface can be achieved. At higher values – 10^6 W/cm^2 – the light thermally affects deeper layers of the material, forming vapour and gas channels. Usually, such
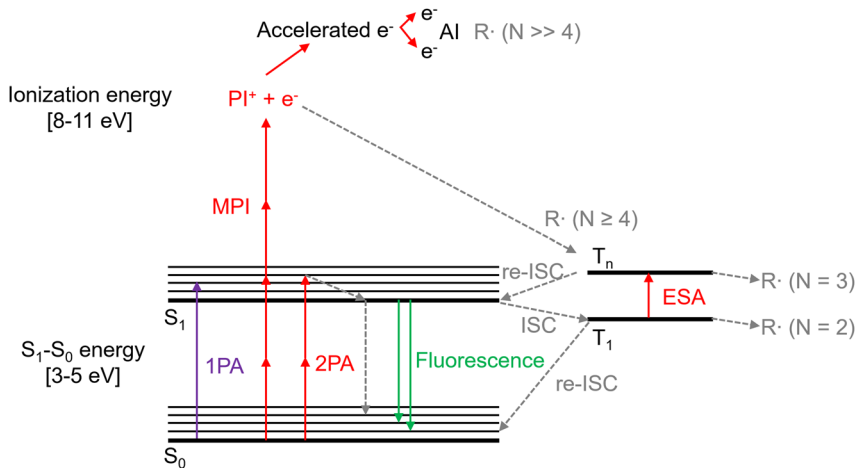
Figure 2: Jablonski diagram. 2PA and MPI are explained in the scheme. 2PA occurs in PI or monomer molecules. They are excited from the ground state S_0 to the excited singlet S_1 state (3–5 eV bandgap) and then through the intersystem-crossing (ISC) go to triplet state where they form radicals. In the MPI case, the electron is separated from the PI or monomer molecules, following avalanche ionization (AI). However, it requires more energy to excite the molecule (e. g., 8–11 eV, four photons). 1PA – one-photon absorption. ESA – excited state absorption. Reprinted with permission from [31].

conditions are applied in laser drilling or welding of the metals. If more than 10^7 W/cm^2 intensity is used, the material can be ablated via vapour or gas phase. However, both vapour and gas are ionized, causing plasma formation. As presented in Table 2, we are aiming in the intensity scale of TW/cm^2 (10^{12}), focused into polymerizable materials. The following section is dedicated to the discussion of photoexcitation under the aforementioned conditions, polymerization steps and its development in a time frame, spatial confinement, heat influence, and main thresholds.

2.1 Photoexcitation

Photopolymerization is a monomers and oligomers bonding reaction, induced via light–matter interaction – photoexcitation. Photoexcitation occurs by absorption of photons. Depending on the amount of the absorbed photons per single excitation event, absorption can be either one-photon (one-photon absorption – 1PA), or multi-photon (multiphoton absorption – MPA) [22]. For example, two-photon polymerization (2PP) is induced via simultaneous absorption of two photons (two-photon absorption – 2PA). Absorption which results in electron transfer into the conduction band can further proceed by gaining energy from the laser pulse and promote the electron to excited states (Figure 2), which also leads to breaking of chemical bonds. This defines a transition from the solid-state response into ionisation which is determined by free electrons or plasma state (sometimes discussed as solid-state plasma to plasma transition). The ionisation proceeds via non-linear processes such as multi-photon ionization (MPI), avalanche ionization (AI), and tunnel ionization (TI). In this section, all the aforementioned non-linear light–matter interactions are discussed.

A prefix "multi" means that more than one photon is absorbed. Depending on the number of absorbed photons, an electron in a valence band can be excited from the ground state S_0 to the higher energy levels states (MPA case) or even can be accelerated to the ionization energy leaving the valence shell (MPI case). Moreover, both MPA and MPI can occur simultaneously as competing processes, also, with possible parallel involvement of 1PA. It might be not easy to define exactly, what is the role of each of the aforementioned phenomena, thus it can be assumed, that only one is dominant while others might be negligible, as they happen on a very different efficiency scale. If after excitation, an electron is transferred to the singlet S_1 state, it is assumed that absorption occurred. It can undergo through the virtual state, when two or more photons are absorbed simultaneously [23], depending on the energy gap between the ground and the excited states. However, the higher order of the non-linear process the higher temporal and spatial photons density is required. For example, 2PA is proportional to the squared optical intensity (I^2). 2PA is shown in the Figure 2, where a Jablonski diagram is used to depict all possible energy pathways that can lead to polymerization. Usually, photoinitiators (PIs) are used to induce photopolymerization reaction. PIs are chemical compounds sensitive to UV/visible light which upon absorption of light form reactive components (free-radicals or photoacids) capable of starting a polymerization reaction. Their bond dissociation energy is in order of 3 eV [24], while monomers require higher energy to induce a cleavage, which can be more than 4 eV [25–27]). Thus, the required intensity I to excite PI molecule is lower compared with monomer or oligomer molecule. Typical values to induce photocleavage are in the order of TW/cm^2. Conventional PIs, however, often suffer from small 2PA cross-sections (σ) in

the near-IR wavelength (λ) range, where femtosecond-lasers are typically used for 2PA induced polymerization [28]. Regular values are less than 10 Göppert Mayer (GM) units, where 1 $GM = 10^{-50}$ [cm^{4}s/molecules/photon] [29]. It results in a low possibility to induce radical formation from PIs molecules. However, considering common 2PP parameters (scanning velocity $v = 100\,\mu$m/s, repetition rate $R = 80$ MHz), it can be calculated that potentially 23 excitation events per molecule can occur [30].

Another way to excite molecules is by MPI. In this case, an electron is separated from the PI or monomer molecule to the unbound state and further process continues via AI. The MPI phenomenon requires one to two orders of magnitude higher I than 2PA (10^{13}–10^{14} W/cm^2) [32]. When a high I ($\approx 10^{14}$ W/cm^2) is used, it might be assumed, that a TI can better describe ionization process than MPI. For comparison, the Keldysh parameter (γ_K) can be calculated, which characterizes the regime in which the processes might occur (TI, if $\gamma_K < 0.5$, or MPI, if $\gamma_K > 0.5$) [33]. The calculated value for high repetition rates and PIs can be found close to 30, which confirms that the MPI process is more likely than TI [30].

When TI can be ignored, it is interesting to establish which of the process (AI or MPI) is dominant. To do so, the density of electrons created by AI (n_e) and by MPI (n_a) must be evaluated:

$$\frac{dn_e}{dt} = n_e w_{\mathrm{imp}} + n_a w_{\mathrm{mpi}}.$$

w_{imp} stands for the avalanche rate and w_{mpi} for the MPI rate [34].

Case study: MPI and AI. The calculations were simulated for the polydimethylsiloxane (PDMS) under two lasers systems: Ti:Sapphire oscillator (pulse duration $\tau = 20$ fs, central wavelength $\lambda = 800$ nm, repetition rate $R = 75$ MHz) and Yb:KGW amplifier ($\tau = 300$ fs, $\lambda = 1030$ nm, $R = 200$ kHz) [18]. Figure 3 represents electron density dependency on the time scale for the avalanche and multi-photon ionizations.

From the graphs, it can be seen that free electrons mainly are generated due to MPI (green line). However, calculated rate in photosensitized PDMS is much higher for the AI ($w_{\mathrm{imp}} = 3772 \times 10^{10}$ s^{-1} > $w_{\mathrm{mpi}} = 5.74 \times 10^{10}$ s^{-1} for Ti:Sapphire system and $w_{\mathrm{imp}} = 374 \times 10^{10}$ s^{-1} > $w_{\mathrm{mpi}} = 2.65 \times 10^{10}$ s^{-1} for Yb:KGW system). The presence of the AI generates enough free electrons to induce optical damage. Moreover, at the high repetition rate which is common in Ti:Sapphire based oscillators (around 80 MHz), accumulative effects (thermal and defects) can occur [5, 35]. Under such circumstances, the polymerization process becomes impossible to control under realistic conditions.
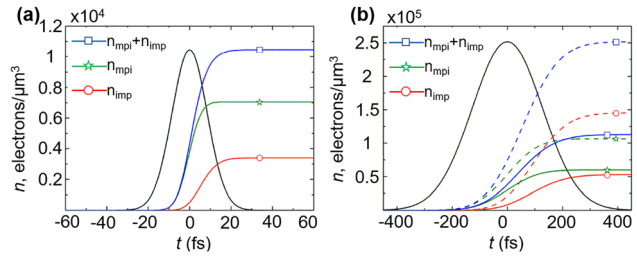

Figure 3: Simulated electron density dependency on time scale for the AI and MPI.
(a) – Ti:Sapphire oscillator system, PDMS + PI. $I = 5.2$ TW/cm^2. (b) – Yb:KGW amplifier system, PDMS + PI. For the continuous lines – $I = 1.2$ TW/cm^2, for the dotted lines – $I = 1.6$ TW/cm^2. Reprinted with permission from [18].

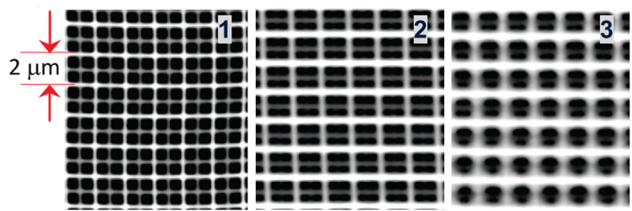**Figure 4:** Scanning electron microscopy (SEM) images of the structures made at the same focusing conditions (13 TW/cm^2) in SZ2080™ pure (1) and doped with 1 wt. % of PI (2 and 3). (1) represents AI case, (2) – AI + 2PP and (3) – 2PP + 1PP. Reprinted with permission from [15].

The experimental results of MPI and AI processes during polymerization are depicted in Figure 4. It shows examples of the three structures made at the same focusing conditions, corresponding to 13 TW/cm^2 for pulse energy 14.5 nJ, but in three different composites: SZ2080™ pure (1) and doped with 1 wt. % of PI (Irgacure 369 (2) and Michler's ketone (3)) [15]. The absence or presence of PI (and PI type), altered the excitation conditions and allowed the demonstration of three different initiation cases: AI, AI + 2PP and 2PP + 1PP, respectively. It can be seen, that the finest spatial resolution was achieved in the non-photosensitized resist. The explanation could be that seeding electrons are produced more efficiently if including 2PP or 1PP cases rather than only AI. Thus, at the considerably higher avalanche rates, as compared to multi-photon, the ionization becomes higher, enabling polymerization via two mechanisms: bond cleavage and thermal accumulation, resulting in increased feature size.

The ionization rate, which is related to the radical generation, has a strong nonlinear character. The linear light–matter interaction defined by the permittivity $\epsilon \equiv \tilde{n}^2$ (or the refractive index $\tilde{n} = n_0 + i\kappa$) is highly altered at the high intensity/irradiance used in 3D laser polymerization

approaching $I_p \sim 1\,\text{TW/cm}^2$. The nonlinear contributions to the real and imaginary parts of the refractive index become significant. An instantaneous ionization following a light intensity envelope is transforming a dielectric material into a metal-like, hence *die-met* material with strongly altered permittivity [36]. The first nonlinear (*I*-dependent) contribution is due to two-photon absorption, which is changing the real part as $n(I) = n_0 + n_2 \times I$ and the absorption coefficient becomes $\alpha(I) = \alpha_0 + \beta \times I$; where the absorption coefficient is related to the imaginary part (extinction coefficient) of the refractive index as $\alpha = 4\pi\kappa/\lambda$. The consequence of permittivity change during laser pulse will affect the absorption depth, which becomes lower in highly excited material. The amount of deposited energy accounts for this change, as discussed further in the section on spatial confinement (Section 2.4).

To summarize, the order of optical nonlinearity in MPL depends immensely on the PI and the conditions used for light excitation [37]. Which way (MPA or MPI) the photoexcitation will proceed, depends on the photosensitive resin's bandgap, which can be tuned using PIs, and selected technical parameters: τ, λ, v, R, and intensity level resulting in the presence or absence of accumulative effects. Currently, the most common light sources have low pulse energies (order of nJ) and high repetition rates (around 80 MHz), yet other options are also possible, as shown in Table 2. One must also note that a sub-300 fs laser pulse width is equally important to the wavelength when determining the type of light–matter interaction. Together they make two distinct cases of sub-100 fs and tens of MHz repetition rates, and above-200 fs and kHz (or a few MHz) repetition rate excitation sources, which determines whether MPA is dominant, or there is significant AI contribution to the energy delivery into the confined specimen volume.

2.2 Polymerization steps

After photoexcitation, PIs reach the triplet state (T_1) by intersystem crossing, and then experience cleavage of the chemical bonds. This action – light-induced cleavage – is called photolysis, or photodissociation. The photolysis reaction can be expressed like this:

$$\text{Photolysis}: \text{PI} \xrightarrow{h\nu} \text{PI}^* \rightarrow \text{R}^* \left(\text{K}^+/\text{A}^-\right),$$
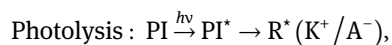
The result of the photolysis is atoms, molecules or ions, that are electrically unstable, thus have the ability to connect other molecules, e. g., monomers. Besides, they are a completely different species than the original PI. Depending on the polymerization class (radical or ionic) it could be free-radicals (R^*) or cations/anions (K^+/A^-). For example, in radical photoinitiating systems, the cleavage happens in aromatic carbonyl compounds that are known to undergo homolytic C–C bond scission upon intense light exposure. This is common for the Norrish type 1 PIs [38]. One more case when the free-radicals can be induced is hydrogen atom transfer reaction with an additional co-initiator molecule. Such systems are Norrish type 2 and usually consist of two components, typically, an aromatic ketone and radical precursor with a weak covalent bond [39]. In photo cross-linking reaction, a combination of any of the following processing parameters: light intensity, temperature, or PI concentration, can improve the rate and extent of curing due to the increase of the number of free radicals available for reaction propagation [40]. The PI concentration is one of the most significant parameters influencing the rate of photopolymerization. However, it has been reported, that the photopolymerization rate increases with the increase of PI concentration, and after reaching an optimum concentration, the rate promptly declines [41]. This is related to the high concentration of primary R^* and is known as a phenomenon called primary radical termination [42]. The decreased curing rate at higher PI concentrations was observed in 1PA induced free-radical polymerization [43]. Moreover, when high light intensities are used (for example, 100–1000 mW/cm^2), a high concentration of primary R^* is established as well. On the other hand, the photopolymerization of photoinitiator-free systems has been reported where bio-derived (meth) acrylate resins were cured by 2PP [44, 45]. Photopolymerization was initiated using ultrashort pulses by MPA, resulting in the cleavage of vinyl double bonds of monomers and generating R^*, which initiated the reaction of (meth)acrylic groups. Synthetic PIs can be toxic [46], thus the elimination of PIs from photoresists enables the prototyping of fully bio-friendly resins. Though, not all systems can undergo the initiator-free photo cross-linking reactions due to the strong bonding of the vinyl group (4.5 eV [25]) to the entire molecule where the double bonds do not cleave generating R^* or K^+/A^-. In this case, PIs are necessary.

After the photolysis occurs, initiation starts and polymerization reaction proceeds to form a cross-linked network. During the initiation, excited R^* or K^+/A^- interact with the monomer then transfers energy and creates a monomeric radical (RM^*) or macrocation/macroanion ($\text{KM}^+\text{X}^-/\text{AM}^-\text{X}^+$). Macrocation/macroanion is joined by a counterion (ion of the opposite charge sign – $\text{X}^{+/-}$) and a pair of ions is formed, which determines the rate of the reaction. Since then the RM^* or $\text{KM}^+\text{X}^-/\text{AM}^-\text{X}^+$ can further continue the interaction with the surrounding monomers, resulting in

longer and longer chains, which has an uneven number of electrons in the valence shell. This step is called chain propagation. The termination of reaction differs for radical and ionic polymerizations. The radical one stops mainly due to a couple of reasons, in which growing RM^* is terminated by other RM^*: recombination or disproportionation. Recombination is a reaction termination when two monomeric radicals merge into a single molecule. Also, the aforementioned primary radical termination might happen. In the case of termination by disproportionation, one proton is transferred from the hydrogen donor radical to the acceptor radical. Thereby, the donor radical is transformed into an unsaturated polymer chain (ending with a $C=C$ double bond), while the acceptor polymer chain is saturated (only $C-C$ single bonds). In ionic polymerization, termination occurs when the macrocation/macroanion transfers a proton (H^+) to the counterion. A neutral molecule is obtained with a double bond at the end. Another case of reaction termination is called chain transfer. It occurs when a proton with a counterion is transferred to another monomer, thus forming a new monomer cation that can further react with the monomers to form a lower molecular weight polymer. Steps of the radical and ionic (depicted cationic case) polymerization reaction are represented in Table 3 [47, 48]. Also, the Table includes common materials, usable for certain type of polymerization, and commercially available resins, based on those materials. Moreover, it is known that the multifunctional monomers and/or oligomers could be employed and cross-linked via dual-curing reactions. The dual-curing reactions such as photo-photo, thermal-photo, photo-thermal, and others take place simultaneously or sequentially [49]. These systems often include two, or more initiators that are activated by heat, different wavelengths or cleave by different mechanisms such as free radical or cationic. An example of a simultaneous dual-curing reaction is the multifunctional acrylate and epoxy monomer system curable under the UV light employing the free radical and cationic PIs leading to the highly photo cross-linked polymer.

The perception of the mechanisms of undergoing photoinduced polymerization reactions is mandatory, as it explains the photo cross-linking kinetics and degree of conversion of this process, presented in the next section. Knowing these factors, availability to design desired photo curable resin for the specific applications is enabled.

2.3 Main factors influencing photopolymerization kinetics and degree of conversion

Photopolymerization, or photo cross-linking, kinetics is crucial in optical 3D printing influencing the ability to prototype material and its usage in additive manufacturing. It defines the occurrence of structural phenomena, such as gelation and vitrification, indicating the moment, when the structural changes have started – the gel point [45]. As mentioned earlier, photopolymerization could be induced via 1PA and MPA via continuous laser irradiation and ultrashort laser pulses, respectively. The 1PA demands less energy, but is a surface polymerization technology, though the strong confinement of the MPA volume enables true-3D freeform structures [50]. As the irradiation intensity defines the photopolymerization induction, it could highly influence the photo cross-linking kinetics as well. Typically, the time taken for the light to propagate through the material is less than 10^{-11} s, while the photochemical reactions and mass transport effects take place over milliseconds or seconds [51]. Therefore, photopolymerization kinetics should be investigated by precise methods such as real-time photorheometry [52, 53], real-time FTIR [54, 55], Raman

Table 3: Equations of radical and cationic polymerizations, used common materials and available commercial resins.

Polymerization steps	Radical polymerization	Cationic polymerization
Photolysis	$PI \xrightarrow{h\nu} PI^* \rightarrow R^*$	$PI \xrightarrow{h\nu} PI^* \rightarrow K^+$
Initiation	$R^* + M \rightarrow RM^*$	$K^+X^- + M \rightarrow KM^+X^-$
Propagation	$RM^* \rightarrow RMM^* \rightarrow \ldots \rightarrow RM_n^*$	$KM^+X^- + M \rightarrow KM_n^+X^-$
Termination	**Primary radical termination:** $RM_n^* + R^* \rightarrow RM_nR$	**Ionic rearrangement:** $KM_n^+X^- \rightarrow KM_n + H^+X^-$
	Recombination: $RM_n^* + RM_m^* \rightarrow RM_{n+m}R$	**Chain transfer:** $KM_n^+X^- + M \rightarrow KM_n + HM^+X^-$
	Disproportionation: $RM_n^* + RM_m^* \rightarrow RM_n + RM_m$	
Common materials	(Meth)acrylates, vinyls, thiols, hydrogels, organic-inorganic hybrid materials	Mostly epoxies
Commercial resins	PEG-DA, PETA, OrmoComp, Ormocer, SZ2080™, PDMS	SU-8, SCR500

spectroscopy [56], photo-differential scanning calorimetry (photo-DSC) [57, 58], voxel onset time (VOT) [59] and other methods. Photopolymerization kinetics refers to the rate of functional groups conversion in time, which promotes a change in polymers' physical properties. Depending on the method used for measurements, it can be depicted variously. In real-time photorheometry kinetics are shown as storage and loss modulus increase in time, which indicates the formation of the 3D polymer network. Real-time FTIR represents changes in absorption spectra before and after curing, revealing the amount (ratio) of functional groups consumed for the polymerization. Raman spectroscopy also reveals the amount of the functional groups before and after polymerization, however, its spectra show scattering of particular Raman active mode, not absorption. Photo-DSC enables monitoring of curing kinetics by measuring enthalpy changes during curing and determining the degree of conversion. VOT demonstrates cross-linked volume growth in time, as well as the cross-linking density due to changes in the refractive index. At the same time, shrinkage, curing depth, and/or monomers diffusion from the adjoining dark regions can also be measured. Both inter- and intramolecular forces affect the rate of polymerization [60]. Vitrification occurs during the photopolymerization process as the degree of conversion (DC) increases followed by the decelerated diffusion of monomers and reduced reaction rates of both propagation and termination [61]. DC is another parameter, which also defines mechanical and physical (refractive index, thermal expansion, etc.) properties of the material [62]. DC characterizes the fraction of bound functional groups as compared to the overall number of functional groups and is measured in %. The higher DC, the harder polymer is. Also, it can be known as degree of the cross-linking or polymerization, double bond conversion. DC is assessed measuring the peak area of absorption or scattering of the double bonds before (A_0) and after (A_t) the irradiation (Equation (1)), which can be measured employing FTIR [54] or Raman spectroscopy [63], respectively.

$$DC = \frac{A_0 - A_t}{A_0} \times 100. \tag{1}$$

UV-curable monomers do not achieve 100% DC due to the steric hindrances and oxygen-induced inhibition leaving residual monomers in the cured volume. The material DC, cured volume, and photopolymerization kinetics could be adjusted by changing the irradiation intensity, exposure duration, amount of PI, and spatial separation of voxels. Going through the literature, achievable typical values of DC approximately alters from 60 to 80% [64, 65], regardless if curing is induced via 1PP or multi-photon lithography (MPL). Sometimes values over 90% are observed,

especially, when additional UV post-curing is applied [66]. Not only inhibition mechanisms [61], but the reaction process and curable resin composition [67] influence DC. In cases of limited mobility of monomers or oligomers, it might be difficult to achieve higher conversion than 50% [63]. Further a couple of **case studies**, how DC can adjust some properties of the material, are given. A. Žukauskas has demonstrated, that the highest value of the refractive index in the SZ2080™ photopolymer was 1.5112, when $DC = 50\%$, and the lowest value was equal to 1.4996 with $DC = 5.5\%$. This represents to change of refractive index up to 1.16×10^{-2} [64]. J. Rys has showed, that Young modulus can be varied in wide range from 10 MPa up to 250 MPa adjusting DC from 24 to 42%, respectively. Additionally, second exposure was applied to the already cured photopolymer. This action helped to reach 20% higher DC values, corresponding to 200% increased Young modulus [62].

Avoiding the decreased curing rate, dual-curing reactions can be applied. For instance, C. Decker et al. [68] demonstrated the synthesis of a bio-derived polymer from a 50:50 mixture (by weight) of 1,6-hexanediol diacrylate (HDDA) and epoxidized soybean oil (ESO) under intense UV irradiation where ESO increased the conversion of HDDA in comparison to a pure formulation. Sequential dual-curing improves the processing and handling as long as the intermediate materials (i.e., after the first curing reaction) are chemically stable and their properties are tailorable [69]. The sequential dual-curing systems are used in several fields where tailored materials and flexible processes are mandatory, e.g. adhesive coatings, lithography, shape-memory materials, and holography [70]. This method was employed in the work of D. Guzman et al. [71] where the thermosets from bio-based compounds were prepared using an efficient environmentally friendly dual click curing methodology resulting in polymers with higher mechanical and thermomechanical performance.

Even though the rate of photopolymerization depends on the number and density of functionalities, their reactivity, and hydrogen bonding, the influence of resin viscosity is dominant. The change of resin viscosity influences the Brownian motion and the diffusion of cleaved PI which affects the photopolymerization process. For example, diffusion of the free-radicals out of polymerization epicentre can cause cross-talk between features written nearby, which is known as proximity effect and is explained in articles [7, 72]. Thus, the influence of the viscosity on the diffusion needs to be discussed. At the highest viscosities, the rate of photopolymerization is the lowest due to the diffusion-limited propagation and termination reactions. As the

viscosity decreases the diffusion limitation is excluded in the propagation reaction then, as the viscosity decreases further, the diffusion limitation is excluded in the termination reaction [73]. In the work of T. Zandrini et al. the influence of the viscosity to the formation of lines in 2PP was investigated (**case study: viscosity influence**) [14]. The experiment was performed in the same two monomers but just different proportions in their concentrations, resulting in four different viscosities (10.4 Pa·s, 116 mPa s, 23 mPa·s, and 15 mPa·s) without affecting reactivity. The higher resin viscosity highly influenced the width of the fabricated lines due to the reduced action of oxygen and the lower probability of termination events because of limited motility. The average value of the smallest measured line width was around 360 nm for the all four resins, meanwhile, decreasing the viscosity from 10.4 Pa·s to 15 mPa·s the maximum line widths were indeed 2.98, 2.31, 1.42, and 0.68 μm. It results in a linear rate of line width growth of almost 90% for the highest viscosity resin and roughly 50% for the lowest one. Exact values can be expressed form the analysis: 7.3, 5.9, 3.3, and 1.74 μm/nJ for resins from 10.4 Pa·s to 15 mPa·s, respectively.

The most common method to control resin viscosity is to change the temperature. At higher temperatures several things occur, affecting the polymerization. At first, viscosity decreases, and the Brownian motion increases enabling the faster free radical migration leading to the prompt active centre occurrence and the higher cross-linking rate [66]. Secondly, the electrons in the monomers accelerate to a more efficient ionization energy, resulting in more free radicals formation [11]. However, at higher temperatures, the oxygen inhibition accelerates due to the increased oxygen diffusion into resin followed by the reduced rate of photopolymerization. Increased temperature causes an increase of propagation and termination rate constants and auto-deceleration delays, leading to longer reaction times before propagation becomes diffusion-limited [74]. Also, the acrylic resin photo cross-linking is an exothermic reaction which generates heat during the photopolymerization reaction [75]. A. Vitale et al. determined that rapid polymerization reactions were the most exothermic and resulted in a larger temperature rise which facilitated the faster traveling front proceeded by accelerating chain propagation during frontal photopolymerization [76]. As the temperature highly influences resin viscosity, oxygen motility, radical diffusion, and termination processes, the polymerization can be affected in different ways. According to K. Takata et al. observed behavior, the voxel size increases while increasing the temperature from −60 to 20 °C and then decreases again in the range of 20−80 °C. Due to enhanced termination at higher temperatures polymer units results in less cross-linked or loose voxels, of which the surrounding portion is easier to be removed in the rinsing process, contributing to the smaller voxel size [77]. On the contrary, Ž. Prielaidas et al. have observed an increment of height and width of the pillars, while increasing the temperature in the range of 20−125 °C, due to increased primary amount of the free radicals [11]. Such a discrepancy might be explained by the two different photoresists and laser systems employed in the aforementioned experiments, leading to the unequal diffusion or accumulative effects and resulting in diverse behavior of the voxel size.

To sum up, photopolymerization kinetics must be well understood for every individual case, in order to achieve the desired goals in additive manufacturing, which simply could be a speed of the process or an optimized spatial resolution, etc. *DC* is of utmost importance, as it affects the physical properties of the polymer; modifying it, can tailor the cured material properties to the desired requirements.

2.4 Spatial confinement

As already mentioned previously, tight spatial confinement is one of the main benefits of the MPL. Thus, in this section, the voxel formation is analyzed.

The employed irradiation intensity profile and its focusing conditions play a key role in the spatial confinement of MPA. The intensity I distribution at the focal plane is usually described as lateral (d_r) and longitudinal (l_z). The indices r and z represent the direction of the beam propagation: radial and axial, respectively. The focusing of the laser beam can be described according to the Rayleigh model. The dimensions d_r and l_z of the laser beam at the focal plane can be described by the equations:

$$d_r = \frac{1.22\lambda}{NA}, \qquad (2)$$

$$l_z = \frac{1.22 n_0 \lambda}{NA^2}, \qquad (3)$$

where n_0 – a real part of the refractive index of the medium (in case of ML – photoresin). λ – wavelength, NA – objective numerical aperture. NA also depends on the refractive index, however, it is of medium between objective and the sample, which can be air or commonly is an immersion oil. For more accurate estimation, the Gaussian intensity distribution at the focal plane must be considered:

$$I(r,z) = I_0 \frac{w_0^2}{w(z)^2} e^{-\frac{2r^2}{w(z)^2}}, \qquad (4)$$

where w_0 and I_0 are radius and intensity at the beam waist. The beam radius can be expressed as:

$$w(z) = w_0 \sqrt{1 + \left(\frac{z}{z_R}\right)^2}.$$

where z_R is a Rayleigh length, which is the distance along the propagation direction of a beam from the waist to the place where the radius enlarges $\sqrt{2}$ times:

$$z_R = \frac{n_0 w_0^2 \pi}{\lambda}.$$

As already was mentioned, MPA will occur when a certain light intensity level is reached. Usually, this is an intensity, when polymerization starts and thus is called polymerization threshold (I_{pt}), which can be expressed the following:

$$I_{pt} = \frac{2P_a T}{R w_0^2 \pi \tau}, \tag{5}$$

where P_a – average power, T – objective transmittance, R – pulse repetition rate, τ – pulse duration. Knowing I_{pt}, d_r and l_z can be specified as [78]:

$$d_r = w_0 \sqrt{\ln\left(\frac{I(r)}{I_{pt}}\right)}, \tag{6}$$

$$l_z = 2z_R \sqrt{\sqrt{\left(\frac{I(z)}{I_{pt}}\right)} - 1}. \tag{7}$$

These equations determine the dimensions of an ellipsoid voxel at the focal plane. Also, it can be expressed in other ways, for example, including such variables as λ, R, n,

exposure duration, and 2PA cross-section and can be found elsewhere [79]. The voxel size can be controlled via the objective NA and other parameters, defining the distribution of the I. Moreover, it is known, that control of I can be implemented by adjusting the amount of the laser light covering the input aperture of the objective [80]. The intensity distribution is presented in Figure 5(a). It shows, how d_r and l_z dimensions alter varying focusing conditions (objective NA), while I is kept constant (calculations were based on Equations (4), (6) and (7)). Polymerization reaction occurs only if I equals or exceeds I_{pt}. Further increasing I, the damage threshold I_{dt} can be reached as the number of free electrons also increases. Above that certain energy threshold, material boiling starts and gas bubbles form. The gap between those two thresholds ($I_{dt} - I_{pt}$) is called the fabrication window (FW). However, it is better to normalize it as to ($I_{dt} - I_{pt}$)/I_{pt} and call it a dynamic fabrication window (DFW) or simply in other words – dynamic range (DR). Figure 5(b) illustrates thresholds and how voxel dimensions d_r and l_z vary according to the applied intensity.

The theoretical evaluation demonstrates that d_r size varies in several hundred nm, while l_z can be obtained in a wider range – from 500 nm to several μm. An interesting fact is that dimensions smaller than the diffraction limit (expressed in Equations (2) and (3)) can be achieved. It can be explained with Equation (4), which says, that there is uneven intensity distribution all over the volume of the voxel. As depicted in Figure 5 part (b), the threshold mechanisms become essential. Within the voxel, just some part of the intensity exceeds the polymerization threshold I_{pt} and induces the reaction in a volume smaller than the rest of the voxel. The polymerization occurs only
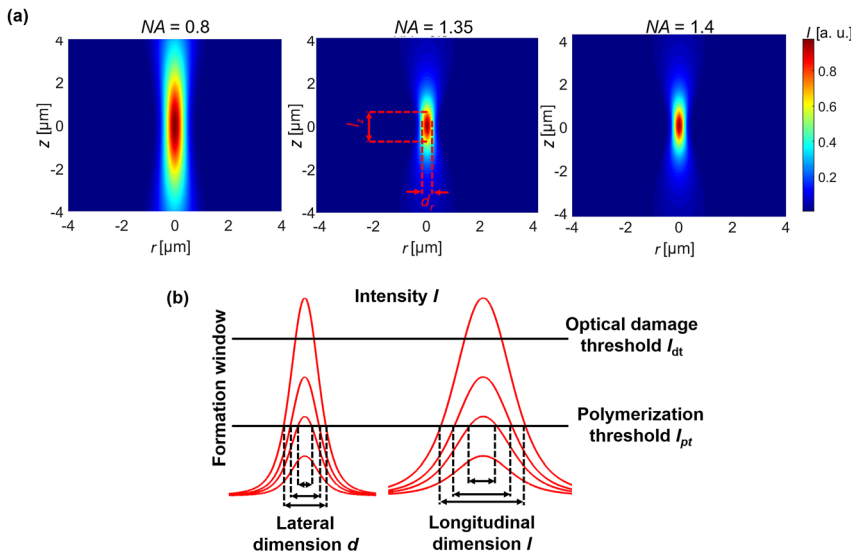

Figure 5: Spatial confinement of light in 2PP. (a) – dynamics of intensity distribution of light focused with an objective lens $NA = 0.8$, $NA = 1.35$ and $NA = 1.4$. Following parameters were used for the calculations: $T = 100\%$, $R = 200$ kHz, $\tau = 300$ fs, $\lambda = 515$ nm, $n_0 = 1.504$. (b) – illustration, how d and l alters when various values of intensity I are applied. Fabrication window is defined by a lower black line (I_{pt}) showing intensity, at which polymerization reaction starts, and an upper one – an optical damage threshold (I_{dt}).

in that certain space, which has enough of the excited chemical species (radicals or cations/anions) to produce sufficient *DC* and withstand the development process in the solvents. This mechanism is defined by Equations (6) and (7), describing how the lateral and longitudinal dimensions of the voxel depend on the applied *I*. Further, some **case studies about feature size** are provided. The authors of different scientific papers have used the advantage of the aforementioned spatial confinement and threshold mechanisms, what enabled them to reach, let's say, a superior line width: F. Burmeister et al. showed nanostructures with dimensions of 91 nm [81], V. Paz et al. achieved 82.5 nm in Zr-hybrid material [82], W. Haske et al. reported up to 65 nm thin lines [83], S. Juodkazis et al. reached 30 nm structures in SU-8 photoresist [84], and D. Tan et al. even sub-25 nm lines in SCR500 [85]. Naturally, here might arise a question, what parameters (usually, average power and scanning speed/exposure duration) and properties of photoresin (for e. g., the concentration of PI) should be chosen to accomplish such small feature sizes? N. Uppal and P. S. Shiakolas tried to answer this question in their work on resolution prediction of MPL [86]. The main findings they made was, that l_z is more sensitive to different levels of P_a, v and concentration of PI, meanwhile d_r can be easily tuned combining low P_a and high v. Both l_z and d_r are more sensitive to power variation than v or PI concentration. Moreover, the authors state that amount of the PI (altering from 3.78 to 4.96%) shows statistical significant effect in the change of d_r only when low power (12.5–16 mW) and slow speed (1 mm/min) is used. From these findings, a conclusion can be delivered, that small feature sizes can be achieved using high scanning speeds, low P_a values and low PI concentration. However, feature size should not be confused with a spatial resolution, which refers to the minimal distance between two resolved features and is limited only by diffraction, while the achievable line width is determined by threshold mechanisms. Additionally, it might be considered, that self-focusing could influence feature size increasing it in a longitudinal direction. Yet, the MPA process causes loss of energy and diffraction. These two conditions create attenuation of the optical beam, due to witch self-focusing is cancelled and does not occur [87, 88]. Moreover, this phenomenon emerges at a certain critical power, which might coincide with optical damage threshold in the polymer, especially when high *NA* objectives are used. In case of the acceleration of 2PP, single voxel size should be increase. For this, the Bessel beam can be applied as it allows to achieve large-volume printing fabricating high-aspect-ratio structures to advance toward a method for layerless

additive manufacturing [89]. The impact of the beam shaping will be discussed more detailed in Section 3.

The absorbed energy and its spatial localization in axial direction of beam propagation is described next. The skin depth in optically excited dielectric material is determined by the imaginary part of the refractive index as $l_{abs} = c/(\omega\kappa) = \lambda/(2\pi\kappa)$ for electric field (E) and $l_{abs}/2$ for the intensity $I \propto E^2$. The absorbed energy density [J/cm^3] at the end of the laser pulse is $W_{abs} = 2AF_p/l_{abs}$, where $F_p = \int_0^{t_p} I(t)dt$ is the integral fluence per pulse, $A = 1 - R$ is the absorbance, R is the reflectance, $I(t)$ is the temporal envelope of intensity. At high excitation in dielectrics, the change of the imaginary part of permittivity is [90]:

$$(\Delta\epsilon_d)_{im} \simeq \frac{\omega_{pe}^2}{\omega^2}\frac{v_e}{\omega} = \frac{n_e}{n_{cr}}\frac{v_e}{\omega}, \qquad (8)$$

where $\omega_{pe} = e^2 n_e/(\epsilon_0 m_e)$ is the cyclic electron plasma frequency, e, m_e are the electron charge and mass, respectively, ϵ_0 is vacuum permittivity, n_e is the electron density, v_e is the electron relaxation frequency (electron-phonon in solid state material), $n_{cr} = \epsilon_0\omega^2 m_e/e^2$ is the critical plasma density at frequency $\omega = 2\pi c/\lambda$; for example at the $\lambda = 1030$ nm the $n_{cr} = 1.05 \times 10^{21}$ cm^{-3} while at its second harmonics $\lambda/2$: $n_{cr} = 4.2 \times 10^{21}$ cm^{-3}. For comparison, at total ionization of air it is still partly transparent for 1030 and 515 nm while water is not according to their molecular densities 2.9×10^{19} cm^{-3} (air) and 3.34×10^{22} cm^{-3} (water). Absorption is increasing with free electron density n_e as

$$\alpha = \alpha_c (n_e/n_{cr})^2 / \sqrt{1 - n_e/n_{cr}},$$

where α_c is the only electron temperature T_e dependent absorption coefficient (plots are shown in ref. [91]). The permittivity at the pre-breakdown in dielectric medium is $\epsilon_d \simeq n_0^2 + i \times (\Delta\epsilon_d)_{im} = n_0^2 + i2n_0\kappa$, where n_0 is the real part of an unperturbed refractive index [90]; index *im* marks the imaginary part. Hence, the skin depth with use of Equation (8) can be expressed as [90]:

$$l_{abs} = \frac{\lambda}{2\pi\kappa} = \frac{n_0\lambda}{\pi(\Delta\epsilon_d)_{im}} = \frac{2cn_0}{v_e}\frac{n_{cr}}{n_e}$$

and is defining localization of the energy deposition along with the beam propagation. The absorbed energy density is then:

$$W_{abs} = A_0\frac{v_e}{cn_0}\frac{n_e}{n_{cr}}F_p \propto \frac{n_e}{n_{cr}}F_p, \qquad (9)$$

where the unperturbed absorbance $A_0 \equiv 4n_0/[(n_0 + 1)^2 + \kappa^2]$. Equation (9) shows that as the electron density n_e is approaching critical plasma density n_{cr}, the most efficient energy deposition occurs. When a nonlinear absorption via

n–photon process generates electrons $n_e \propto I_p^n \sim F_p^n$, it begins to saturate as the critical density is approached. When the dielectric breakdown is reached ($\epsilon_d \equiv 0$), the volume behaves as a metal where the absorbed energy is proportional to the fluence, $W_{\mathrm{abs}} \sim F_p$ at $n_e = n_{cr}$ (Equation (9)). Interestingly, that a two-photon absorption with $n_e \propto F_p^2$ (i.e., the nonlinearity of absorption $N = 2$) will result in $W_{\mathrm{abs}} \sim F_p^3$ (Equation (9); not $\sim F_p^2$) dependence due to increasingly lower energy absorption as electronic excitation is approaching the critical density. Since 3D laser fabrication via polymerization, structural damage, nanogratings formation, etc., occurs in strongly localised volume, the energy absorbed in that volume (its density W_{abs}) is the most relevant parameter as compared with fluence or intensity $F_p \propto I_p$. Shallow energy deposition is also important for the laser ablation which is the most efficient in the burst mode of with small pulse energy and high repetition rate of MHz-to-GHz (in the burst) [92] when 3D removal of material approaches controlled evaporation. Interestingly, the material removal is dependent on the pulse energy E_p with characteristic second order slope $N = 2$ which is characteristic of direct absorption ($N = 1$) in electron generation according to Equation (9).

Spatial confinement was discussed in this section. It describes what the smallest features can be produced employing MPL and explains its nature. Modification of material, polymerization or structural damage, is determined by the absorbed energy density (in volume) which is dynamically changing during the pulse following intensity envelope. With a generation of free carriers, absorption is increasing and cause an increasingly shallower energy deposition (the absorption skin depth) as the density of plasma is approaching the critical. This is the mechanism of energy localization for a specific modification: localized polymerization, melting, evaporation, dielectric breakdown. The shorter the pulse, the more precise control of the absorbed energy at the focal volume can be mastered.

2.5 Heat conduction

It is known that thermal effects like local heating and heat conduction have a strong influence on the resulting machining quality for many laser machining processes [93]. In the case of 2PP, thermal effects are not so obvious as MPA is a photochemical process. It is assumed, that heat during photopolymerization originates from different phenomena: accumulated and then dissipated energy from 2PA or 1PA (if available), and exothermal reaction. However, heating might still have a not-desired influence, for example, causing a less-controlled process and resulting in resolution loss. Therefore, heat flows from the voxel to the surrounding needs to be discussed. It can be described with the following equation:

$$\tau_c = \frac{c_p \rho}{4\kappa} l_c^2,$$

where τ_c is a cooling time for a given cooling distance l_c, ρ is mass density, c_p specific heat, and κ heat conductivity [94]. It gives a good estimate for the typical distance covered by the heat flow within a certain time and vice versa. $\frac{c_p \rho}{\kappa} = 10^7 \frac{s}{m^2}$ for monomers. Taking common parameters of 2PP used in J. B. Müller Ph. D. dissertation, $R = 80$ MHz (or 12.5 ns between pulses, what corresponds to τ_c) and 200 fs pulse duration, the assessed cooling distance would be $l_c = 70$ nm. It is less than a focused beam radius (165 nm), which means, that applying a sequence of pulses, the heat will accumulate. However, typical exposure durations usually are more than 200 fs and can span up to ms. In this case, l_c increases up to 20 μm.

Case study: conductivity and temperature distribution. A comparison between the simulated conduction behavior for Gaussian intensity distribution and actual experiment. It was evaluated, that no cooling happened between the 200 fs pulses, separated in 12.5 ns time, resulting in the thermal accumulation. The Figure 6 demonstrates two situations when a single pulse or multiple pulses (approximately continuous exposure) heating occurs. If we assume that there is no heat conduction, heat will accumulate. If conduction present, the peak temperature in the centre of the laser focus starts to saturate after around 100 ns. After 1 ms, the peak temperature increases to a value which is roughly 15 times higher than the average temperature increase due to a single pulse. On the other hand, heating by one single pulse, the peak temperature indeed decays within roughly 100 ns, indicating that this is the relevant time-scale for conductive cooling to occur. More theoretical calculations were conducted previously. For example, N. Uppal and P. S. Shiakolas presented a mathematical model describing the effect of temperature increase on the diffusion and reaction kinetics of the polymerization process, comparing dynamics between 80 MHz and 1 kHz repetition rate femtosecond laser systems. The output of this work was that using laser systems with high R (80 MHz), dark period of the reaction becomes much shorter than the duration of the molecular diffusion (12.5 ns $vs.$ μs-ms), resulting in accumulation of heat and radicals, as well [95]. Other research groups have performed experiments investigating thermal effects during

2PP. The presented results are in good agreement with the aforementioned numerical analysis. One of the methods to assess thermal accumulation is the evaluation of the dimensions or shape of objects being formed. It was demonstrated by the Račiukaitis group, who have conducted research on pulse width (35 ns *vs* 300 ps) and repetition rate (0.5 kHz *vs* 1 kHz) influence on the laser interference lithography [96]. According to them, when long pulses (ns) or higher repetition rate (1 kHz) are employed, thermal accumulation causes thermal polymerization, resulting in the taller and wider structures. One more scientific publication describing spatial resolution dependency on repetition rate, but this time in bursts manner, was published by T. Baldacchini [97]. They have observed that when using the same laser fluence, polymer lines fabricated at different burst repetition rates had different dimensions. In particular, the widths of lines become smaller with decreasing burst repetition rates. The authors believe that this phenomenon can be explained if heat accumulation is considered as a part of the 2PP process. Another approach to assess heat accumulation is temperature measurements from the luminescence of upconverting nanoparticles. According to two reports of such measurements, for a common and typical photoresist, the temperature increases 30 ℃ [98] or only a few degrees [94] under relevant writing conditions during 2PP and up to hundreds of degrees in overexposing regime. These experimental values coincide with other theoretical simulations, performed by T. P. Onanuga [99]. According to his calculations, a quasi-linear dependence of temperature with laser power was observed within polymerization regime. In the damage regime, the nonlinear temperature increase was monitored, which can be attributed to plasma formation due to avalanche ionization.

Summarizing this Section, it is evident, that thermal effects can not be neglected in MPL technology, as it has influence as in other machining processes. Laser systems with high repetition rate leave no time for the material to cool, affecting the polymerization mechanisms and feature size.

2.6 Thresholds in MPL and their formation

MPL is a deterministic process influenced by the earlier discussed phenomena. Thus, we consider this technology to have threshold processes due to several reasons and at several stages. The first one is based on physical fundamentals of nonlinear light absorption – an **Intensity Threshold, [W/cm²]** (described in Sections 2.1 and 2.4). It is necessary to obtain a sufficient amount of intensity to induce 2PA, MPI, or both processes. Then it is important to generate an ample number of excited molecules to exceed the inhibition mechanisms and proceed with the polymerization. The numerical value of the required intensity can be determined using Equation (5) for the polymerization threshold. Increasing I, more radicals can be generated, but the optical damage threshold I_{dt} should not be exceeded. To avoid damage, the concentration of the radicals can be controlled via an appropriate quantity of
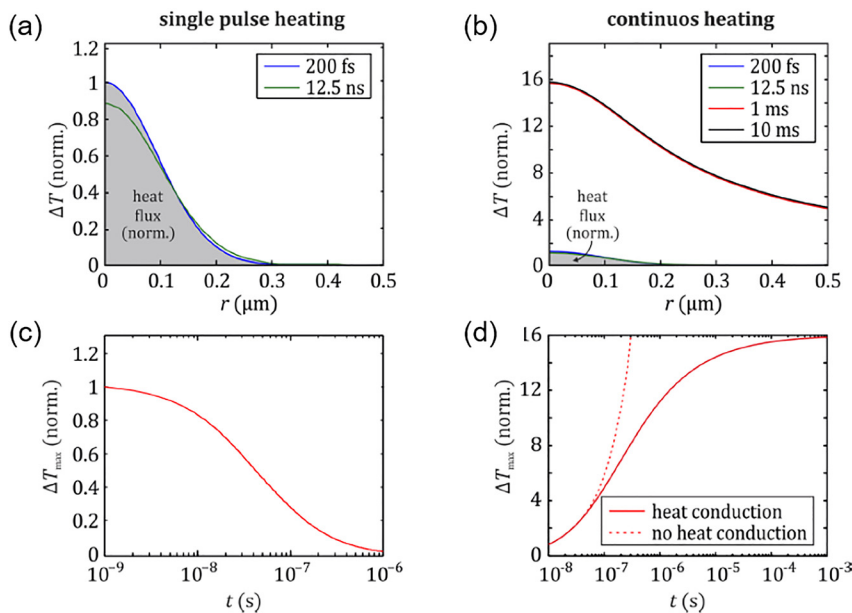

Figure 6: Calculated temperature distribution at selected moments in time (a, b) and calculated peak temperatures as a function of time (c, d). The incoming heat flux is indicated by the gray areas. As the absolute magnitude of the temperature change is unknown, all curves are normalized to the temperature change due to one single pulse.
(a) – conductive broadening of the temperature distribution after one single pulse, directly after the end of the exposure and at the beginning of the subsequent pulse. (b) – conductive broadening of the temperature distribution for a continuous heat source after typical exposure periods. (c) – change of a peak temperature after a single pulse exposure. (d) – change of a peak temperature in the case of a continuous heat source. Reprinted with permission from [30].

energy, which can be called energy dose – D [J]. The dose can be evaluated as energy density expressed with Equation (9), however, it is much easier to calculate dose which comes from the laser irradiation without assessing absorption of the material and the area or volume of the interaction. Simply, D can be expressed as:

$$D = t_{\exp} R E_p^N.$$

Where $t_{\exp}$ is exposure duration, R repetition rate, E_p laser pulse energy, and N the degree of nonlinearity of the absorption. As 2PP is a second-order process ($N = 2$), D is proportional to E_p^2 (corresponding to I^2). As the laser irradiation intensity exceeds the threshold value I_{pt} to initiate the polymerization, D further can be controlled via adjustment of other formation parameters such as $t_{\exp}$ (which is proportional to scanning velocity v) or R. In such a manner the size of the features can be precisely controlled [81]. If I_{pt} is not reached, even after high exposure energy densities (2.8 J/cm^2) no polymerization occurs [100]. It is worth mentioning, when talking about intensity threshold, I_{pt} is usually expressed as average power per surface unit ($I = \frac{P_a}{S} = \left[\frac{W}{cm^2}\right]$) or for energy fluence as D per surface unit ($F = \frac{D}{S} = \left[\frac{J}{cm^2}\right]$) [101, 102]. However, the polymerization occurs in the volume, thus it would be more accurate to estimate I_{pt} or D per volume ($I_v = \frac{P_a}{V} = \left[\frac{W}{cm^3}\right]$ or $F_v = \frac{D}{V} = \left[\frac{J}{cm^3}\right]$). Continuing further on the thresholds in MPL, monomers and oligomers chains interconnect and form a polymer network. If a polymer network achieves a critical DC, making it solid from liquid, it becomes not soluble in an organic solvent and can withstand the development process. This is important as some small size features can be manufactured and observed while they are in monomer surrounding, however, after developing they might vanish. Moreover, this condition is important as it describes the mechanical and physical properties of the polymerized material. As DC is ensured via chemical reactions through the cross-linking of double bonds (see Section 2.3), we name this threshold **Cross-linking Threshold (ratio of % in converted/not converted species)**. It determines how many excited individual molecules have to be converted into a polymer chain to survive the solvent during the development. Again, it becomes valid only once the Intensity threshold is exceeded. The last condition is related to the resulting individual features and structures. First of all, the volume of the objects at the nanoscale will greatly influence its mechanical properties. Secondly, it is dramatically changing whether the objects remain on the substrate after the development procedure or not, will highly depend on its type (2D, 2.5D or true 3D) architecture

and aspect ratio of the single unit (for e. g., width and height of the line) or the filling ratio of the whole object, surface area between object-substrate, tension forces, uniform or non-uniform shrinkage [103, 104]. To overcome the aforementioned issues, additional pre- or post-processes must be taken into account. For example, supportive structures might be used to reduce deformation of the object, shape pre-compensation needs to be evaluated to receive desired dimensions object [105], UV or thermal treatment applied to fully cure the material [106, 107], supercritical CO$_2$ drying employed to reduce surface tension and fix the object [103]. Due to these additional technical solutions, we call this threshold an **Engineering Threshold**. It can be evaluated using the superimposition of the produced objects with its original model. If there are inaccuracies between the model and manufactured sample, the aforementioned technical actions can be used to achieve more defined features or structures.

Three types of thresholds were determined in this section. The first one is based on photoexcitation mechanism via MPA and depends on applied irradiation intensity. The second one threshold is derived from chemical aspects of the reaction and is fulfilled when sufficient DC is achieved. The last threshold is the one, which depends on the user and sample architecture the most and is called Engineering.

3 Wavefront engineering

Conventionally, the multi-photon 3D-structuring process proceeds by sequentially scanning point-by-point, so building up the three-dimensional shape a single point at a time. This process is inherently slow and does not allow for the transition of LDW-MPL to production, rather than a just prototyping tool, which is mainly used for scientific research. Besides, the resolution is completely material-dependent, and cannot be altered by just employing better focusing optics or sophisticated exposure strategies. As, however, the capabilities of the MPL technology are unique, a lot of research effort has been spent engineering the laser beam wavefront to increase both the resolution and the productivity of the technique. In the following paragraphs, we will describe how the resolution can increase by employing the principles of stimulated-emission depletion (STED) microscopy, and the productivity can increase by changing the shape of the laser beam, or by employing multiple laser beams.

3.1 Multi-photon lithography inspired by STED

While MPL is the only technique that can produce readily assembled 3D structures with sub-micron features, its resolution lags behind competing technologies such as electron and focused ion beam lithographies as well as nano-tip scanning techniques [108], where sub-10 nm resolution is considered routine. To address this, STED multiphoton lithography inspired by STED fluorescence microscopy was developed [109]. In MPL inspired by STED, two laser beams are used: one is used to generate the radicals that initiate photopolymerization, and the second beam to deactivate them. The radical switching increases not only the feature dimensions but also affects the resolved distance between distinct features (Figure 7).

Different methodologies have been demonstrated including MPL where the deactivation beam is the same color [111], or different color [109, 110, 112] with the activation beam. A 1PP scheme has also been demonstrated [113], as well as a quencher diffusion, all chemical methods [114]. In addition to increasing the resolution, the possibility to shape the deactivating beam allows the very precise control of the voxel shape and, therefore, the polymerization shape. The smallest feature recorded using MPL inspired by STED is 9 nm [115]. While MPL inspired by STED showed a lot of promise at the beginning, and some very high-resolution nanostructures were produced [116], its application turned out to be very complicated and cumbersome, basically allowing the employment of only specific materials dedicated to the processing itself, with only a few groups adopting it.

3.2 Needle beams

Traditionally for some applications, a longer working distance or high aspect ratio nanostructures are required. For this purpose, it is useful to employ a needle beam rather than a Gaussian beam [117]. Two types of needle beams have been employed in MPL: Bessel beams and ring-Airy beams: while at the beginning they might appear similar, in contrast to Bessel beams, ring-Airy beams exhibit almost invariant voxel dimensions and shapes as a function of the focus position; they can, therefore, be employed to increase the working distance significantly [118]. Bessel beams can be generated easily using axicon lenses, however, their shape and size cannot be altered [119, 120]. A more convenient and flexible method is to use a spatial light modulator (SLM), to engineer the laser beam wavefront to the desired shape, allowing the dynamic, on-demand modification of the voxel shape, size and working distance [118, 121, 122].

3.3 Many beam and holographic 3D printing

Changing the shape of the beam can reduce the time required to build specific architectures, it is not, however, a universal tool. To revolutionize 3D printing productivity, one needs to be able to either built a whole object using a single or small number of laser pulses or to write several objects at the same time using many beams (see Figure 8(a)). The potential of using more than one beams for parallel micro-fabrication was recognized soon after the first demonstration of MPL [123]. It has been demonstrated
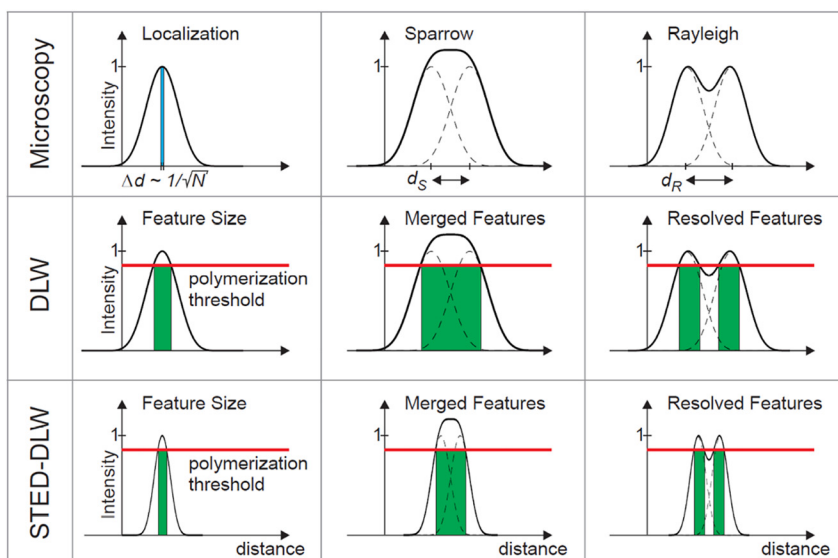

Figure 7: A graphical representation of how two-colour lithography works, and comparison with STED Microscopy.
The first column shows a localization of a single object with accuracy determined by the square root of the number of detected photons, the second column – Sparrow limit, the third – Rayleigh limit of resolution. Green area represents a solidified part of the polymer, that can withstand development. Reprinted with permission from [110] ©The Optical Society.

using microlens arrays [123, 124], diffractive optical elements (DOEs) [125, 126], SLMs [127, 128], and digital micromirror devices (DMDs) [129]. In most cases, parallel microfabrication has been employed to make distinct objects with a resolution of a few microns. Using parallelly-fabricated micro-objects τo create a larger object was until recently not demonstrated; recent work, however, by KIT [125] and INL [126] using DOEs have demonstrated some beautiful stitching in 3D mechanical metamaterials and scaffolds for cell growth (Figure 8(b)). In these cases, the DOE is used to create multiple beams, while the motion system scans the desired pattern, moving either the beam or the sample. The main disadvantage of this method is that it can generate only periodic structures.

To overcome this, and enable free-form rapid 3D printing via MPL, holographic projection is needed. Holographic 3D printing is considered the Holy Grail of MPL, and a lot of research efforts have been spent on this [131, 132] (Figure 8(c)). The idea is simple: print a whole object in one, or a burst of laser shots. Implementation, however, is not so simple: research has shown that its application is hampered by speckle, i.e., laser hot spots that produce unwanted artefacts [133]. Also, the available projection hardware, SLMs, and DMDs have low fluence damage thresholds and do not allow the holographic printing of large areas in single laser shots, and bursts of shots or breaking up the image is required [134].

A recent report in Science demonstrated 3D printing using a tomographic reconstruction scheme where a complex volume was manufactured by using many numerically estimated tomographic projections of the object design [135]. It is possible that adapting this method to enable multi-photon absorption would address these problems and enable high resolution, holographic MPL. More technical details about the aforementioned writing strategies are covered in a recent review by W. Lin [136], where certain printing techniques are described with their feasible setups and what objects or structures can be

manufactured with each of them. In brief, these strategies are derived from a light–matter interaction of a single voxel [125], whether it is beam paralelization [130], interference [12], dynamic projection [134], or in a combination with synchronized sample translation [102].

4 Material engineering (organics, hybrids, renewables, functionalized)

The materials (organic or composite) that are used nowadays in 3D structuring by MPL are similar to those employed in conventional lithographic applications. The system comprises two main components, the polymerizable material, which will produce the 3D structure, and a photoinitiator, which is a molecule that absorbs light and provides the active species which initiate the polymerization. To date, a large variety of polymeric and hybrid materials, as well as photoinitiators have been used in MPL. These are mostly negative photoresists [137–139], in which the light exposed area becomes polymerized or cross-linked to produce the solidified 3D structure, allowing the unexposed resist to be washed away in the development stage. Positive photoresists [140], in which the light beam exposure leads to chain scission, creating shorter units that can be dissolved and washed away in the development process, have been also employed. Regardless of the material being a negative or positive photoresist, it should fulfil the following requirements: (i) it should be transparent at the wavelength of the laser beam used for the 3D structuring, to allow the focusing of the laser within the volume of the material, (ii) it should possess a fast curing speed to enable the structuring at a reasonable scanning speed and (iii) after curing the material should present chemical and mechanical stability to produce robust and
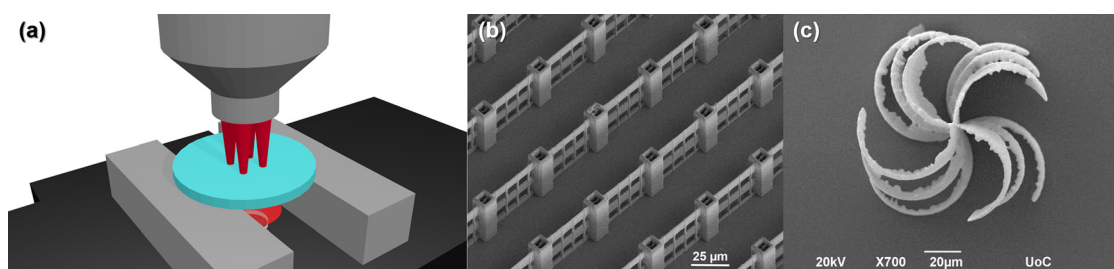

Figure 8: (a) – A depiction of multi-focus illumination after the magnification objective. Reprinted with modification from [130]. (b) – 3D microstructures fabricated in parallel using 9×9 beamlets created by a fixed DOE. Reprinted with permission from [126]. (c) – A 3D object printed holographically. Reprinted with permission from [131].

well-defined 3D structures. In the following sections, we will discuss four main classes of materials used as negative photoresists in MPL, namely organic, renewable, hybrid, and functional materials.

4.1 Organics

Following the development of the multi-photon absorption theory in 1931, its application in the 3D structuring of materials using lasers was applied in the photopolymerization of (meth)acrylate monomers [141]. This monomer class is particularly attractive for use in multi-photon polymerization because it combines the following properties:

1. There is a great variety of commercially available organic acrylates bearing different functionalities;
2. They are transparent at visible and near-infrared wavelengths, which means that these materials do not absorb light linearly at these wavelengths, and can, therefore, be processed by infrared and green ultra-fast lasers;
3. They can be polymerized fast, exhibiting low shrinkage upon polymerization, to produce mechanically and chemically stable structures;
4. They can be developed in common, non-aggressive solvents, such as isopropanol, ethanol, acetone, etc.

A wide range of negative tone, acrylate-based photosensitive materials for 2PP have been developed and commercialized by Nanoscribe GmbH. These enable the fabrication of highly accurate structures with optical quality surface roughness, the construction of millimeter-sized objects at high speed, as well as the manufacturing of complex 3D designs with submicron features of high aspect ratios and low shrinkage. Additional advantages include the biocompatibility and low autofluorescence of some of these resins which render them attractive in the biomedical field. Due to their specialized properties, these materials have been proposed for use in applications ranging from micro-optics [142, 143], diffractive optical elements [144, 145], microfluidics [146], microelectromechanical systems (MEMS) [147] and in life sciences [148].

Among the first organic materials used in MPL is SU-8. It is a negative tone photoresist comprising monomer units bearing eight epoxy groups as the bulk building material and a triaryl sulfonium salt as the photoacid generator (PAG) [149]. The PAG undergoes a photochemical reaction which results in the acid-catalyzed cross-linking of the epoxy monomer units. Upon a subsequent post-baking step, solidified structures are created. The SU-8 resist has been used in multi-photon lithography for the fabrication

of microrobots [150], MEMs [151], microfluidic devices [152, 153], etc., but is also widely used in the microelectronics industry in combination with soft lithographic methods [154].

Another important class of organic materials used in MPL is the one based on hydrophilic monomers or polymers leading to the formation of hydrogels. A hydrogel is defined as a 3D network of hydrophilic polymers that can swell in water retaining a large amount of the solvent ($\geqslant$10%) [155]. Hydrogels possess a network structure with flexibility very similar to that of natural tissues, property that renders them particularly attractive for biomedical applications [156]. Among the most extensively studied hydrophilic polymers is poly(ethylene glycol) (PEG). PEG-based photoresins have been widely used for the preparation of 3D hydrogel structures for cell growth using MPL [157–159]. These hydrogel structures demonstrate excellent biocompatibility and even allow the encapsulation of living cells during the fabrication process [160, 161].

In addition to the aforementioned, widely used, organic photoactive materials, several other organic materials have been utilized in MPL, including poly(vinyl alcohol), poly(lactic acid), trimethylolpropane ethoxylate triacrylate and commercial resists (i.e., Accura®SI10, eShell, and SCR-701).

4.2 Renewables

All the above-mentioned examples comprise synthetic organic materials. Another major class of photo-structurable organic materials is the one based on natural biopolymers. Over the past decade, renewable materials have attracted a great deal of attention from researchers as substitutes for petroleum-derived materials. Since scientists and industry developed and optimized the methods of extraction, purification, and modification of renewable raw materials, these materials became increasingly accessible and easier applicable in optical 3D printing [162]. Tabletop 3D SLA/DLP printers were the first printers to be used to make 3D objects from biobased materials. The following renewable materials were successfully applied in SLA and DLP: epoxidized linseed oil [163], modified gelatin [164, 165], acrylated epoxidized soybean oil [166], vanillin [167, 168], camphene [169, 170], isosorbide derivatives [171], and others. The study of the biobased materials for 3D SLA/DLP printers focused mainly on the kinetics of photo cross-linking and mechanical properties of the printed material, while a more detailed study of a wider range of biobased materials was performed with the subsequent introduction of MPL. Due to the wider possibilities to

control the parameters, MPL technology enabled photo cross-linking of more complex biobased systems which were not possible to apply in 3D SLA/DLP printers [172]. The reason why natural polymers have been employed in MPL is the need to produce 3D structures that resemble the natural cell environment, with the most promising candidates being proteins and polysaccharides which are basic constituents of the cell's extracellular matrix (ECM). Protein-based 3D constructs display exceptional biocompatibility and are suitable for cell culture studies and tissue engineering [173]. The natural biopolymers that have been most widely used, so far, in MPL are bovine serum albumin [174], gelatin [175], collagen [176], fibrinogen [177] and chitosan [178]. These macromolecules can be structured by MPL using appropriate cross-linker molecules, which chemically bind onto two or more functional groups present on the biopolymer chains. The active groups of the biopolymers arise from their structural units, i.e., amino acids, and include primary amine ($-NH_2$), carboxylic acid ($-COOH$), thiol ($-SH$), and carbonyl ($-CHO$) functionalities. Complex microstructures have been already produced from modified thymol [179], cellulose-based compounds [180], functionalized gelatin and chitosan blends [178], silk-based compounds [181, 182], hyaluronic acid [183], and dextran derivatives [184]. Even photoinitiator-free systems of biobased materials [44, 45] were applied in MPL technology, which has made it possible to eliminate toxic photoinitiators commonly used in photo cross-linking reactions. Thus, MPL technology has made it possible to expand the use of renewable raw materials in cell scaffolding manufacturing that mimic realistic cell environments for use in regenerative medicine towards tissue engineering.

4.3 Hybrid materials

Over the last two decades, MPL material research has focused on the development of photosensitive hybrid composites. These hybrid organic-inorganic materials constitute an important class of materials in which both inorganic and organic structural elements co-exist in atomic or nanoscale dimensions. Their very interesting aspect is that they also combine the dissimilar properties of their constituents. The inorganic part enhances the mechanical and thermal stability of the hybrid, modulates its refractive index, and contributes specific electronic, redox, electrochemical or chemical properties. On the other hand, the organic part provides the possibility to tune the mechanical properties, control the porosity and connectivity of the network, and confers specific chemical, physical or

biological properties. Typical and most widely used hybrid materials for MPL are ORMOCER®, OrmoComp®, and SZ2080™.

ORMOCERs (Organic Modified Ceramics) have an inorganic silicon dioxide (SiO_2) backbone functionalized with acrylate or epoxide groups, which can be employed to cross-link the bulk resin material, with the use of a photoinitiator, into the solid 3D structures [185, 186]. The ORMOCER® material is provided by Microresist Technologies, Germany, and combines the desired features of sol-gel processing with an organic polymer, providing opportunities for the MPL preparation of various 3D models for applications that range from photonics to tissue engineering [187–191].

OrmoComp® is very similar to ORMOCER® and is also commercially available from Microresist Technologies. It incorporates an inorganic SiO_2 network and tunable organic functional units providing tailored material properties for selected applications. Following UV curing, OrmoComp® offers glass-like material properties. Among its benefits, there are high transparency, excellent mechanical properties, and chemical stability [192]. Apart from the above-mentioned properties, OrmoComp® is also biocompatible and has attracted great interest for microfabrication applications in a broad range of bio-related fields, including tissue engineering [193, 194], drug delivery [195], microfluidic systems [196] and bio-inspired surfaces [197].

Although ORMOCER® and OrmoComp® have been extensively studied by numerous groups, the microstructures fabricated from these materials suffer from extensive shrinkage during the development process, in which solvents are used to remove the unpolymerized material. To overcome such distortions, new hybrid materials based on metal alkoxide precursors based on silicon and other metals were developed in IESL-FORTH. The most common material is SZ2080™, which is commercially available from IESL-FORTH upon request. This hybrid material first undergoes a sol-gel process to form the inorganic network, followed by the photo-polymerization of the organic functional groups to produce a material that resembles glass and possess superior resistance to shrinkage along with chemical and mechanical stability. The material has been used for the fabrication of nano- and micrometer-sized structures for applications in micro-optics [198, 199], photonics [138, 200, 201], MEMS [202], tissue engineering [203–205], metamaterials [206, 207], pyrolysis [208] and more. Besides the Zr-based hybrid, materials using Titanium [209], Vanadium [210], and Germanium [211] metals have been also developed.

4.4 Functionalized

As stated above, MPL can potentially find applications in optics, sensing, imaging, MEMs, and tissue engineering. Nowadays, the growing number of applications require a wider range of materials to achieve the targeted functions. Besides the well-defined 3D structures, most applications require functional properties that are manifest in controlled chemical, mechanical, optical, electronic, or biological interactions with the environment. Following the growing demand for advanced applications, great efforts have been dedicated to the functionalization of materials that are applicable in MPL. The approaches to integrate specific properties or functions into the 3D microstructures comprise the (i) use of functional precursors and (ii) post-MPL functionalization. In the first approach, the material is formulated in such a way, that is, at the same time, suitable for direct fabrication of 3D structure using MPL and contains one or more additives that enrich the final structure with targeted functionality. In post-fabrication functionalization, a conventional photosensitive material is used to create the 3D structures, and post-fabrication chemistry or physical deposition processes are used to create functionalities onto the 3D structure. Both organic and hybrid materials have been used to alter the properties of the 3D fabricated structures.

Several routes have been employed to create active 3D structures. Fluorescent 3D organic microstructures have been fabricated using acrylate monomers doped with fluorescent dyes or via post-fabrication chemical functionalization [212, 213]. Doping with fluorescent dye yields active structures that can be used for sensing, photonics, or biomedical applications [214, 215]. Chromophores have also been used for inducing non-linear effects [216]. A recent trend to avoid the disadvantages of dyes employs the use of quantum dots as the fluorescent probes [217, 218], or non-linear species for the realization of switching devices [219]. Electrically conductive microstructures have been also realized by doping organic materials with carbon nanotubes [220] or by blending poly(ethylene glycol) diacrylate (PEG-DA) with 3,4-ethylenedioxythiophene (EDOT) [221]. Bulk metal oxides have been used with organic or hybrid materials to form composites by blending. Metal oxides confer mechanical hardness, large and often tunable refractive index, wide optical bandgap, high or low electrical resistivity depending upon the structure and its composition, and ferromagnetism. Moreover, metal oxide nanoparticles have been used for their promising electronic properties, which can be exploited in cancer treatment, chemical, bio-sensing, and photovoltaics [222–225].

Metals can also be used to create structures that possess high electrical and thermal conductivity, high mechanical strength, good optical reflectivity, and other novel properties [226–231].

The functionalization of materials used for 3D structuring by MPL has been studied for biomedical applications. Functionalization with proteins [232] and thymol [179] are only two examples that have been reported very recently.

4.5 Shrinkage

Materials shrinkage during MPL is a major issue, as normally strict dimensional accuracy is required. Volume shrinkage can cause a large build-up of internal stress [233], which results in defects formation [234], and dimensional changes, responsible for the formation of micro-cracks and deteriorated mechanical properties [235]. The shrinkage occurs during the polymerization reaction as the liquid resin turns into a dense cross-linked network leading to the change of intra- and intermolecular distance (details in Figure 9). The formation of C−C covalent bonds (~1.54 Å in length) from C=C double bonds (~1.33 Å in length) brings expansion in intramolecular level, but at the same time, the transformation from intermolecular distances (~3–5 Å in length) connected via weak Van der Waals force into the typical C−C strong covalent distance leads to the shrinkage, whose value is found to be 2 to 3 times bigger than the expansion, and the shrinkage is observed [236]. As a case example could be an atomistic model of ORMOCER® material, presented in the publication by S. Fessel [237]. Simulations of the densities of the unpolymerized and polymerized material were performed. It was assessed that density increment (which corresponds to the polymerization shrinkage) upon polymerization was around 1.9–4.1%, and was in good compliance with the experimental value −3.8%.

The shrinkage during photopolymerization could be controlled or reduced by the changed UV-curing conditions, the addition of an inert component, adjustment of the monomer structure, applied ring-opening polymerization, usage of the thiol-containing system and hybrid system (e.g., free-radical/cationic hybrid system, thiol-ene/acrylate hybrid system, and organic/inorganic hybrid system), and adopting solid-state photopolymerization [238]. For **case study: shrinkage** there is an example of 1PA induced polymerization, described in T. T. Taubock et al. [239] paper. They have investigated the influence of modulated photoactivation on axial polymerization shrinkage and shrinkage force employing different
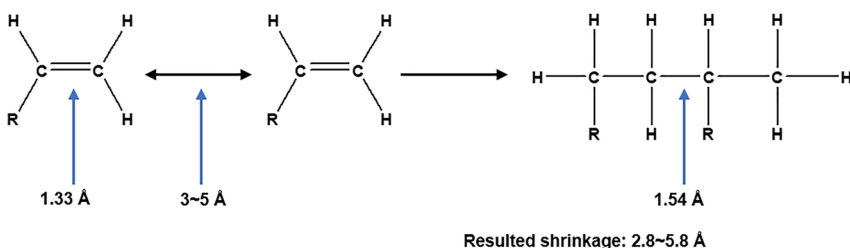
Resulted shrinkage: 2.8~5.8 Å

Figure 9: Change of distance in the polymerization. Originally in [238].

irradiation protocols with identical energy density (27 J/cm^2): high-intensity continuous light, low-intensity continuous light, soft-start, and pulse-delay curing. The results showed that pulse delay curing (3 s at 300 mW/cm^2 → Delay (3 min) → 29 s at 900 mW/cm^2) was effective in reducing shrinkage force formation in comparison to continuous high-intensity irradiation (30 s at 900 mW/cm^2) without affecting hardening and axial polymerization shrinkage. Moreover, it is known, that the narrowed intermolecular distance of monomers by the crystallization process before the photopolymerization can reduce the shrinkage efficiently. Monomers closely packed into crystal cells pre-shrink during the crystallization process and the post-polymerization shrinkage is reduced [240]. However, due to the mobility restrictions photopolymerization in the solid-state leads to the decreased functional group conversion and gradual polymerization rate. This is the reason, why the most high-end photoresists for 3D optical laser lithography are liquid [241]. Moreover, the shrinkage can be reduced via material composition. Hybrid materials, presented in Section 4.3, or thiol/acrylate mixtures are great candidates for reduced shrinkage [67].

To conclude this chapter, it is worth it to stress out, that since the MPL was presented as a new additive manufacturing technique till nowadays plenty photocurable resins were investigated, developed and even commercialized. Diversity of the materials have brought.

5 Substrates, post-exposure development and processing

In the previous sections, MPL was discussed from different perspectives: light–matter interaction, including fundamentals of physics and chemistry, beam and material engineering. As it was presented, all these "variables" defines the limits and applicability of the MPL. Although being essential matters, it is not the only things characterizing this technology. The surface on which 3D structures are being patterned has great importance, thus the substrate must be selected properly. Additionally, the post-exposure processing with UV light or heat treatment can open new horizons breaking the limits of convenient MPL.

5.1 Substrates

Various substrates can be used for direct MPL 3D patterning: glass [34] and all other dielectrics (amorphous and crystalline) [20], semiconductors [17], metals [242], coatings [243] and other polymers [188]. The surface of the substrate can be optically transparent, opaque, or reflective, any shape or surface roughness and waviness, including such widespread platforms as microfluidic channels [244], tubes, and other 3D scaffoldings, fiber tips [199], CMOS chips [245], etc. Also structuring without any substrate or artificial sacrificial structures can be realized – this enables the manufacturing of integrated and free objects [204]. The ability to flexibly perform fabrication on, in or no (without) substrate makes the MPL technique exceptional in rapid prototyping for scientific research and advantageous as an integration tool for industrial production.

5.2 Post-processing

As several parameters influence the rate of photopolymerization and polymer properties during the polymerization process, post-print processes are also crucial to obtain the quality product. Post-processing after the photopolymerization commonly consists of unreacted monomer removal using solvent (e.g., ethanol, isopropanol, acetone, 4-methyl-2-pentanone, tetrahydrofuran, etc. or their mixtures), often followed by UV-curing and/or thermal post-curing to raise conversion and increase of the cross-linking density [106]. UV/thermal treatment allows us to accelerate 2PP for prototype production through profile/contour scanning, in which only the outer surface is

produced via 2PP leaving behind an interior of uncured resin [246]. An inevitable presence of unreacted monomer is observed due to the conversion gradient, which appears because of the non-uniformly exposed single space units caused by a technological implementation, for example, layered production in 1PP and point-by-point voxel writing in 2PP. The unreacted monomer could be removed with a quick solvent "rinse", to eliminate surface monomer, or a longer "soak" to eliminate monomer from the interior of the 3D printed part [199, 247]. For instance, in the bulky object produced via 1PA mechanism, solvent "rinse" does not create visual changes in the surface, though leaves the monomers retained in the volume causing plasticization, which decreases the modulus of the printed part [248]. Opposite, solvent "soak" removes unreacted monomer efficiently though conversion-dependent shrinkage, creating a saw-tooth corrugation at the surface, which causes stresses within the printed part. In particular, delicate micro- or nano-scaled structures suffer from insufficient mechanical stability against capillary forces which mainly arise in the fabrication process during the evaporation of the developer and rinsing liquids. To overcome this issue, custom designed development is being explored. J. Purtov et al. suggest an improved development, which includes gentle replacement of the developer-monomer-mixture with isopropanol, while structures are kept immersed during the whole procedure. Then the structures are further cross-linked by additional UV exposure, rinsed once again, and dried in the air [249]. Another well-known way to eliminate the capillary forces is supercritical CO_2 drying. Since this process removes surface tension while rinsing the microstructures, sophisticated 3D microstructures such as a microcantilever, a high-aspect-ratio submicron pillar of 500 nm in diameter, and 50 μm in height and a lattice model can be obtained without harmful deformation [103].

The shrinkage during polymerization and uneven, distinct layers after prototyping and post-processing could be avoided employing coarse-grained models that can accurately predict the patterning process. A. Vitale et al. used two 3D printing parameters, the light absorption coefficient and a reaction conversion rate constant, in addition to a (fixed) conversion threshold for solidification ϕ_c to optimize the printing process and accurately control the monomer-to-polymer conversion profile of each layer and that of the entire printed object [76]. Created models optimizing the printing process facilitate to avoid the shrinkage and eliminate the empirical optimization of printing parameters.

5.3 Heat treatment

Case study: downscaling and material conversion. The MPL is unique for its 3D structuring and advantageous in high resolution, yet sometimes even finer features/dimensions are required. Also, functional devices would benefit from being inorganic. For instance, for photonic and metamaterial applications the MPL made 3D structures can be successfully downscaled, feature size reduced or both using pyrolysis, plasma etching, and a sequential combination of both, respectively (Figure 10(a)) [250]. Furthermore, starting with hybrid organic-inorganic pre-polymer one can perform pyrolysis or calcination to sinter the object till partial or full evaporation of organic constituents (Figure 10(b)). Extended heating durations at elevated temperatures enables converting the material into an amorphous glass or even crystalline ceramic substances [20]. Such templating expands the applications in photonics as the resizing of the object also results in material densification which in turn influences the refractive index [251] and improves the mechanical properties like strength and ductility [252].

To summarize, availability of the various substrates, post-processing steps, and heat treatment enhances and makes MPL more versatile technology, expanding its throughput, spatial resolution, material accessibility, and produced objects structural complexity.

6 Current applications

The driving force for each technology and its validity of impact is judged by the benefits of applications. The current advances in MPL already enable its immediate usage in creating tailored mechanical metamaterials [253, 254].

The impact fields are intertwined and benefiting from individual advances, for instance, metamaterials [255] are being applied for tissue engineering applications [256] as the scaffold performance are being studied with human cells already [257]. The most immediate applications are within the field of micro-optics [245, 258] and telecommunications [207, 259]. It might be either single units, like lenses (or matrices of the repeated element), or complex architecture assemblies, consisting of different components. Moreover, using advanced techniques, such as subsurface controllable refractive index via beam exposure, volumetric gradient index lenses and waveguides can be fabricated [260]. More sophisticated advances are implemented in the field of integrated chips
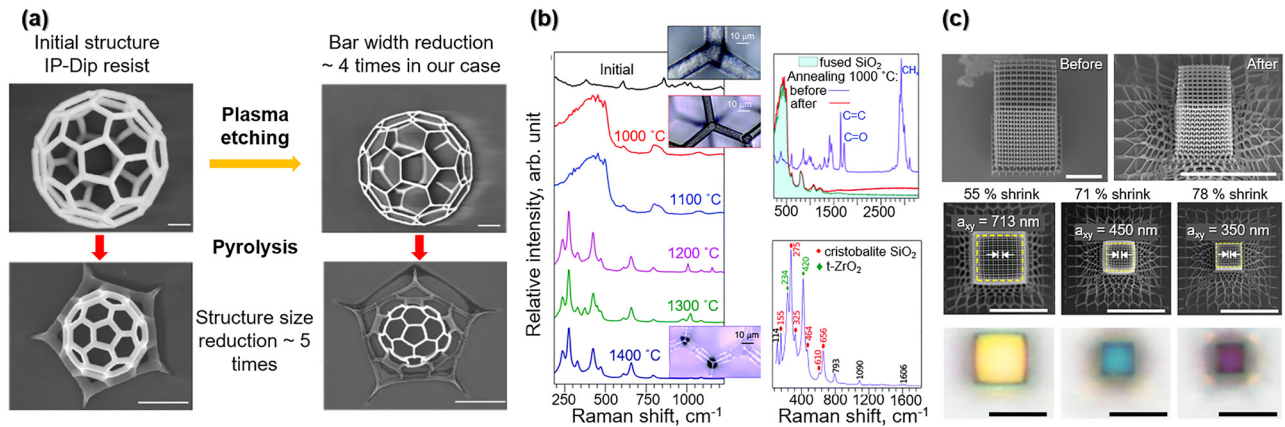
Figure 10: Thermal post-processing of structures, manufactured via MPL.
(a) – down-scaling and feature size reduction using plasma etching, pyrolysis or both. Scale bars represent 1 μm. Reprinted with permission from [250]. (b) – material conversion from hybrid via inorganic amorphous to crystalline. The graph on the left shows the change in the Raman spectrum at several annealing temperatures, the upper graph on the right depicts the detailed spectrum of the initial structure and the heat treated structure in comparison to fused silica, lower one demonstrates Raman spectrum after the highest temperature (1400 °C) annealing with peak matching to cristobalite and tetragonal zirconia (t-ZrO$_2$). Reprinted with permission from [20]. (c) – photonic function enhancement via isotropic shrinking. The first row is tilted SEM images of a representative woodpile photonic crystal before and after heating, the second and third rows are SEM images and corresponding brightfield reflection-mode optical micrographs of the woodpile photonic crystal with different shrinkage, respectively. Scale bars represent 10 μm. Reprinted with permission from [251].

[244] and programmable materials engineering [261]. MPL is a suitable tool for the manufacturing of 3D micromachines. Movable microparts such as micropumps or manipulators can be produced. Applying external forces, for example, laser irradiation or a magnetic field, these micromachines can be controlled remotely, making them applicable in functional microfluidic systems for biology and analytical chemistry [262]. Recently, it was shown
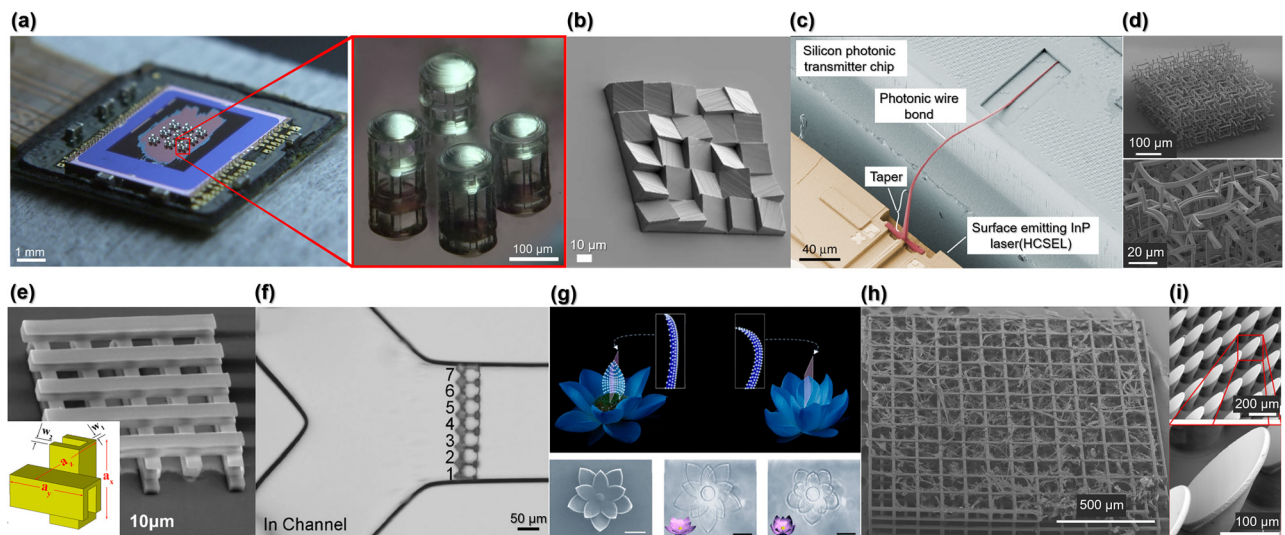

Figure 11: Examples of applications.
(a) – An array of micro-objectives on CMOS chip. Reprinted with permission from [245]. (b) – SEM image of 3D printed DOE (prism array). Reprinted with permission from [258]. (c) – Photonic wire bond. Reprinted with permission from [259]. (d) – A negative thermal expansion coefficient metamaterial structure. Reprinted with permission from [255]. (e) – 3D split-cube resonator metamaterial. Reprinted with permission from [207]. ©(2020) American Chemical Society. (f) – A microfluidics chip integrated into a glass channel. Reprinted with permission from [244]. (g) – An actuating micro-flower as a programmable material. Scale bars represent 10 μm. Reprinted with permission from [261]. (h) – SEM image of a 3D scaffold with cell culture for *in vivo* studies (courtesy of S. Rekštytė). Details of the research can be found here [257]. (i) – SEM images of anisotropic dry adhesive PDMS microstructures. Reprinted with permission from [268].

that scanning-probe microscopy (SPM) engines consisted of cantilevers, tips, a wide variety of actuator and read-out elements can be produced employing MPL. It is expected, that MPL could enable a mass fabrication of SPM arrays, which is unavailable by current approaches [263]. Combining MPL with electrochemical deposition, thermal evaporation, or sputtering truly arbitrary 3D design magnetic nanostructures (magnetic nanowires, multi-segmented nanowires, nanotubes, etc.) can be produced [264]. Using metal-salt-based photoresins, direct metal writing can be achieved, which is used in sensing, catalysis, and nanoelectronics fields [265]. Compared with standard micromachining methods for electronics, for example, electron beam lithography, which is a multi-step process, time-consuming and costly, fewer procedures are required employing MPL [266]. Few more applications where MPL can be used is surface treatment towards biomimetic structures. The replication and modification of surface allow obtaining desired properties, for instance: superhydrophobicity, friction enhancement by adhesion, and drag reduction. Those features correspond to nature-based topographies (lotus leaf, frog toes, and shark skin, respectively). Such and similar surface treatments can be achieved via MPL, as presented in Maddox et al. paper [267, 268].

Versatile application areas were discussed here. A few of them are visualized in Figure 11, including the case examples of metamaterials, micro-optics, photonics, DOE, micro-fluidics, programmable materials, and tissue engineering. All the mentioned and depicted applications confirm the convenience, advantages, and perspectives of MPL technology.

7 Conclusions and perspectives

As it was covered, not all light–matter interaction mechanisms are clearly explained and there is still lots of space for scientific studies to reveal underlying phenomena. Yet, the technology is developing rapidly and enabling true 3D printing without a limit on its scale or the type of material. Multi-scale lithography employing single bio-derived resin has been recently demonstrated, filling the gap of scales created by the feature dimensions fabricated via linear and non-linear absorption processes [269]. A facile multi-material 3D manufacturing strategy was validated as well [270]. Finally, heat-treatment post-processing enabled true inorganic structures without geometrical or dimensional restrictions [20]. The next decade seems to be not less interesting than the past one from a research point of view.

Furthermore, establishing the technique into industrial lines of production for micro-optics, nano-photonics, telecommunications, (bio-)scaffolds, microfluidic chips, metamaterials, and smart-materials will be an interesting challenge. The field will benefit from the fact that the only way to densify the functionalities is to fold the structure into the third and fourth-dimensions.

The evolution of fs-lasers is entering burst-mode operation which allows for higher energy extraction from photo-excited solid-state media (crystal, glass) balancing on the optical breakdown limit (but not reaching it). We are using the very same phenomenon of optical excitation and free-electron generation at the vicinity of optical breakdown for optical 3D structuring of materials. For polymerization and thermal modification, the irradiance just below an optical breakdown is harnessed, while for the ablation, the irradiance at the breakdown conditions is employed. The very same approach of the burst mode which is tailored to spare the source of laser radiation at the maximum excitation is employed to excite the solid-state material (work-piece) to the desired conditions of controlled phase transition: melting, evaporation, or plasma formation. Protocols required for the maximum of the extracted luminous energy from the laser crystal in the burst mode are expected to be best tailored to control the laser ablation, polymerization, etc., which are most efficient close to the runaway dielectric breakdown. Electronic excitation of material controls the absorption efficiency in 3D by defining the depth of energy deposition and can be well controlled only for the ultra-short laser pulses. This is a key distinction of fs-laser technology which together with wavefront engineering advances makes it future-ready.

Conflict of interest statement: The authors declare no conflict of interest.

References

[1] M. Malinauskas, M. Farsari, A. Piskarskas, and S. Juodkazis, "Ultrafast laser nanostructuring of photopolymers: A decade of advances," *Phys. Rep.*, vol. 533, no. 1, pp. 1–31, 2013.

[2] M. Miwa, S. Juodkazis, T. Kawakami, S. Matsuo, and H. Misawa, "Femtosecond two-photon stereo-lithography," *Appl. Phys. Mater. Sci. Process*, vol. 73, pp. 561–566, 2001.

[3] M. Thiel, J. Fischer, G. von Freymann, and M. Wegener, "Direct laser writing of three-dimensional submicron structures using a continuous-wave laser at 532 nm," *Appl. Phys. Lett.*, vol. 97, p. 221102, 2010.

[4] D. Perevoznik, R. Nazir, R. Kiyan, et al., "High-speed two-photon polymerization 3D printing with a microchip laser at its fundamental wavelength," *Opt. Express*, vol. 27, no. 18, pp. 25119–25125, 2019.

[5] M. Malinauskas, P. Danilevičius, and S. Juodkazis, "Three-dimensional micro-/nano-structuring via direct write polymerization with picosecond laser pulses," *Opt. Express*, vol. 19, no. 6, p. 5602, 2011.

[6] E. T. Ritschdorff and J. B. Shear, "Multiphoton lithography using a high-repetition rate microchip laser," *Anal. Chem.*, vol. 82, pp. 8733–8737, 2010.

[7] M. T. Do, T. T. N. Nguyen, Q. Li, H. Benisty, I. Ledoux-Rak, and N. D. Lai, "Submicrometer 3D structures fabrication enabled by one-photon absorption direct laser writing," *Opt. Express*, vol. 21, no. 18, pp. 20964–20973, 2013.

[8] G. Witzgall, R. Vrijen, E. Yablonovitch, V. Doan, and B. J. Schwartz, "Single-shot two-photon exposure of commercial photoresist for the production of three-dimensional structures," *Opt. Lett.*, vol. 23, pp. 1745–1747, 1998.

[9] W. H. Teh, U. Durig, U. Drechsler, C. G. Smith, and H. J. Guntherodt, "Effect of low numerical-aperture femtosecond two-photon absorption on (SU-8) resist for ultrahigh-aspect-ratio microstereolithography," *J. Appl. Phys.*, vol. 97, no. 5, p. 054907, 2005.

[10] P. Mueller, M. Thiel, and M. Wegener, "3D direct laser writing using a 405 nm diode laser," *Opt. Lett.*, vol. 39, no. 24, pp. 6847–6850, 2014.

[11] Ž. Prielaidas, S. Juodkazis, and E. Stankevičius, "Thermal control of SZ2080 photopolymerization in four-beam interference lithography," *Phys. Chem. Chem. Phys.*, vol. 22, no. 9, pp. 5038–5045, 2020.

[12] E. Stankevičius, E. Daugnoraitė, and G. Račiukaitis, "Mechanism of pillars formation using four-beam interference lithography," *Opt. Laser Eng.*, vol. 116, pp. 41–46, 2019.

[13] S. Maruo, O. Nakamura, and S. Kawata, "Three-dimensional microfabrication with two-photon-absorbed photopolymerization," *Opt. Lett.*, vol. 22, no. 2, pp. 132–134, 1997.

[14] T. Zandrini, N. Liaros, L. J. Jiang, et al., "Effect of the resin viscosity on the writing properties of two-photon polymerization," *Opt. Mater. Express*, vol. 9, no. 6, p. 2601, 2019.

[15] M. Malinauskas, A. Žukauskas, G. Bičkauskaitė, R. Gadonas, and S. Juodkazis, "Mechanisms of three-dimensional structuring of photo-polymers by tightly focussed femtosecond laser pulses," *Opt. Express*, vol. 18, no. 10, p. 10209, 2010.

[16] B. Stender, F. Hilbert, Y. Dupuis, A. Krupp, W. Mantei, and R. Houbertz, "Manufacturing strategies for scalable highprecision 3D printing of structures from the micro to the macro range," *Adv. Opt. Technol.*, vol. 8, nos 3–4, pp. 225–231, 2019.

[17] A. Žukauskas, M. Malinauskas, A. Kadys, et al., "Black silicon: substrate for laser 3D micro/nano-polymerization," *Opt. Express*, vol. 21, no. 6, p. 6901, 2013.

[18] S. Rekštytė, "The Development and Applications of the Methods of Direct Laser Writing Using Femtosecond Light Pulses in Transparent Cross-Linkable Materials," PhD thesis, Vilnius, Vilnius University, 2016, p. 133.

[19] P. Kiefer, V. Hahn, M. Nardi, et al., "Sensitive photoresists for rapid multiphoton 3D laser micro- and nanoprinting," *Adv. Opt. Mater.*, vol. 2000895, pp. 1–14, 2020.

[20] D. Gailevičius, V. Padolskytė, L. Mikoliūnaitė, S. Šakirzanovas, S. Juodkazis, and M. Malinauskas, "Additive-manufacturing of 3D glass-ceramics down to nanoscale resolution," *Nanoscale Horiz.*, vol. 4, no. 3, pp. 647–651, 2019.

[21] J. Zhu, Y. Chen, S. Xie, L. Zhang, C. Wang, and R. Tai, "Nanofabrication of 30 nm Au zone plates by e-beam lithography and pulse voltage electroplating for soft x-ray imaging," *Microelectron. Eng.*, vol. 225, p. 111254, 2020.

[22] M. Göppert-Mayer, "Über Elementarakte mit zwei Quantensprüngen," *Ann. Phys.*, vol. 401, no. 3, pp. 273–294, 1931.

[23] M. Farsari, G. Filippidis, and C. Fotakis, "Fabrication of three-dimensional structures by three-photon polymerization," *Opt. Lett.*, vol. 30, no. 23, pp. 3180–3182, 2005.

[24] X. Allonas, J. Lalevee, and J. P. Fouassier, "New advances in the investigation of photoinitiator reactivity," *Tech. Conf. Proc. – UV EB Technol. Expo Conf.*, pp. 547–553, 2004.

[25] K. A. Savin, "Radicals and radical anions," in *Writing Reaction Mechanisms in Organic Chemistry*, 3rd ed., Indianapolis, Eli Lilly and Company, Butler University, 2014. Chap. 5, pp. 237–292, https://doi.org/10.1016/b978-0-12-411475-3.00005-1.

[26] J. Fischer, J. B. Mueller, J. Kaschke, T. J. A. Wolf, A.-N. Unterreiner, and M. Wegener, "Three-dimensional multi-photon direct laser writing with variable repetition rate," *Opt. Express*, vol. 21, p. 26244, 2013.

[27] E. Stauffer, A. J. Dolan, and R. Newman, "Review of basic organic chemistry," in *Fire Debris Analysis*, 3rd ed., Burlington, Academic Press, 2008. Chap. 3, pp. 49–83, https://doi.org/10.1016/B978-0-12-663971-1.X5001-5.

[28] K. J. Schafer, J. M. Hales, M. Balu, K. D. Belfield, E. W. Van Stryland, and D. J. Hagan, "Two-photon absorption cross-sections of common photoinitiators," *J. Photochem. Photobiol, A*, vol. 162, nos 2–3, pp. 497–502, 2004.

[29] S. C. Ligon, R. Liska, J. Stampfl, M. Gurr, and R. Mülhaupt, "Polymers for 3D printing and customized additive manufacturing," *Chem. Rev.*, vol. 117, pp. 10212–10290, 2017.

[30] J. B. Müller, *Exploring the Mechanisms of 3D Direct Laser Writing by Multi-photon Polymerization*, PhD thesis, Karlsruhe, Karlsruher Instituts für Technologie, 2015, p. 153.

[31] J. B. Mueller, J. Fischer, and M. Wegener, "Reaction mechanisms and in situ process diagnostics," in *Three-Dimensional Microfabrication Using Two-photon Polymerization*, Oxford, Elsevier, 2016. Chap. 3, pp. 82–101, https://doi.org/10.1016/B978-0-323-35321-2.00005-4.

[32] S. M. Hankin, D. M. Villeneuve, P. B. Corkum, and D. M. Rayner, "Nonlinear ionization of organic molecules in high intensity laser fields," *Phys. Rev. Lett.*, vol. 84, no. 22, pp. 5082–5085, 2000.

[33] B. Chimier, O. Utéza, N. Sanner, et al., "Damage and ablation thresholds of fused-silica in femtosecond regime," *Phys. Rev. B*, vol. 84, no. 9, pp. 1–10, 2011.

[34] J. Stampfl, R. Liska, and A. Ovsianikov, *Multiphoton Lithography – Techniques, Materials and Applications*, Weinheim, Wiley-VCH Verlag GmbH & Co. KGaA, 2017, p. 408.

[35] A. M. Alshehri, K. L. N. Deepak, D. T. Marquez, S. Desgreniers, and V. R. Bhardwaj, "Localized nanoclusters formation in PDMS upon irradiation with femtosecond laser," *Opt. Mater. Express*, vol. 5, p. 858, 2015.

[36] E. G. Gamaly and A. V. Rode, "Ultrafast re-structuring of the electronic landscape of transparent dielectrics: new material states (Die-Met)," *Appl. Phys. A*, vol. 124, no. 278, 2018, https://doi.org/10.1007/s00339-018-1693-3.

[37] N. Liaros and J. T. Fourkas, "The characterization of absorptive nonlinearities," *Laser Photonics Rev.*, vol. 11, no. 5, p. 1700106, 2017.

[38] Z. Wang, "Norrish type I reaction," in *Comprehensive Organic Name Reactions and Reagents*, Hoboken, NJ, USA, John Wiley & Sons, 2010, pp. 2062–2066.

[39] E. Andrzejewska, "Photopolymerization kinetics of multifunctional monomers," *Prog. Polym. Sci.*, vol. 26, no. 4, pp. 605–665, 2001.

[40] A. Yebi, B. Ayalew, S. Pilla, and X. Yu, "Model-based robust optimal control for layer-by-layer ultraviolet processing of composite laminates," *J. Dyn. Syst-T. ASME*, vol. 139, pp. 021008–11, 2017.

[41] Z. Doğruyol, N. Arsu, S. K. Doğruyol, and Ö. Pekcan, "Producing critical exponents from gelation for various photoinitiator concentrations; A photo differential scanning calorimetric study," *Prog. Org. Coating*, vol. 74, no. 1, pp. 181–185, 2012.

[42] M. D. Goodner and C. N. Bowman, "Modeling primary radical termination and its effects on autoacceleration in photopolymerization kinetics," *Macromolecules*, vol. 32, no. 20, pp. 6552–6559, 1999.

[43] J. P. Fouassier and J. Lalevée, "Basic principles and applications of photopolymerization reactions," in *Photoinitiators for Polymer Synthesis*, Wiley-VCH Verlag GmbH & Co. KGaA, 2012, pp. 1–1, https://doi.org/10.1002/9783527648245.part1.

[44] K. Parkatzidis, E. Kabouraki, A. Selimis, et al., "Initiator-free, multiphoton polymerization of gelatin methacrylamide," *Macromol. Mater. Eng.*, vol. 303, no. 12, pp. 1–6, 2018.

[45] M. Lebedevaite, J. Ostrauskaite, E. Skliutas, and M. Malinauskas, "Photoinitiator free resins composed of plant-derived monomers for the optical μ-3D printing of thermosets," *Polymers*, vol. 11, no. 1, p. 116, 2019.

[46] C. G. Williams, A. N. Malik, T. K. Kim, P. N. Manson, and J. H. Elisseeff, "Variable cytocompatibility of six cell lines with photoinitiators used for polymerizing hydrogels and cell encapsulation," *Biomaterials*, vol. 26, pp. 1211–1218, 2005.

[47] J. F. Rabek and J. P. Fouassier, *Radiation Curing in Polymer Science and Technology*, Andover, Springer, 1993, p. 563.

[48] A. Žemaitaitis, *Polimerų fizika ir chemija*, Kaunas, Technologija, 2001, pp. 239–296.

[49] X. Ramis, et al., "Click-based dual-curing thermosets and their applications," in *Thermosets: Structure, Properties, and Applications*, 2nd ed., Elsevier, 2018, pp. 511–541, https://doi.org/10.1016/B978-0-08-101021-1.00016-2.

[50] H. H. Duc Nguyen, U. Hollenbach, U. Ostrzinski, K. Pfeiffer, S. Hengsbach, and J. Mohr, "Freeform three-dimensional embedded polymer waveguides enabled by external-diffusion assisted two-photon lithography," *Appl. Opt.*, vol. 55, no. 8, p. 1906, 2016.

[51] M. R. Gleeson, S. Liu, J. Guo, and J. T. Sheridan, "Non-local photo-polymerization kinetics including multiple termination mechanisms and dark reactions: part III primary radical generation and inhibition," *J. Opt. Soc. Am. B*, vol. 27, no. 9, p. 1804, 2010.

[52] M. Lebedevaite, J. Ostrauskaite, E. Skliutas, and M. Malinauskas, "Photocross-linked polymers based on plant-derived monomers for potential application in optical 3D printing," *J. Appl. Polym. Sci.*, vol. 137, no. 20, p. 48708, 2020.

[53] A. Navaruckiene, E. Skliutas, S. Kasetaite, et al., "Vanillin acrylate-based resins for optical 3D printing," *Polymers*, vol. 12, no. 2, p. 397, 2020.

[54] Q. Chen, Q. Yang, P. Gao, B. Chi, J. Nie, and Y. He, "Photopolymerization of coumarin-containing reversible photoresponsive materials based on wavelength selectivity," *Ind. Eng. Chem. Res.*, vol. 58, no. 8, pp. 2970–2975, 2019.

[55] C. T. W. Meereis, F. B. Leal, and F. A. Ogliari, "Stability of initiation systems in acidic photopolymerizable dental material," *Dent. Mater.*, vol. 32, no. 7, pp. 889–898, 2016.

[56] T. Baldacchini, M. Zimmerley, C.-H. Kuo, E. O. Potma, and R. Zadoyan, "Characterization of microstructures fabricated by two-photon polymerization using coherent anti-Stokes Raman scattering microscopy," *J. Phys. Chem. B*, vol. 113, pp. 12663–12668, 2009.

[57] Y. C. Kim, S. Hong, H. Sun, et al., "UV-curing kinetics and performance development of in situ curable 3D printing materials," *Eur. Polym. J.*, vol. 93, pp. 140–147, 2017.

[58] I. Saenz-Dominguez, I. Tena, M. Sarrionandia, J. Torre, and J. Aurrekoetxea, "Effect of ultraviolet curing kinetics on the mechanical properties of out of die pultruded vinyl ester composites," *Compos. Appl. Sci. Manuf.*, vol. 109, pp. 280–289, 2018.

[59] S. Engelhardt, J. Tempeler, A. Gillner, and M. Wehner, "The voxel onset time as a method for the evaluation of two photon lithography," *J. Laser Micro Nanoen.*, vol. 8, no. 3, pp. 230–233, 2013.

[60] H. Kilambi, J. W. Stansbury, and C. N. Bowman, "Deconvoluting the impact of intermolecular and intramolecular interactions on the polymerization kinetics of ultrarapid mono(meth)acrylates," *Macromolecules*, vol. 40, no. 1, pp. 47–54, 2007.

[61] K. Taki, Y. Watanabe, H. Ito, and M. Ohshima, "Effect of oxygen inhibition on the kinetic constants of the UV-radical photopolymerization of diurethane dimethacrylate/photoinitiator systems," *Macromolecules*, vol. 47, no. 6, pp. 1906–1913, 2014.

[62] J. Rys, S. Steenhusen, C. Schumacher, C. Cronauer, and C. Daraio, "Locally addressable material properties in 3D micro-architectures," *Extreme Mech. Lett.*, vol. 28, pp. 31–36, 2019.

[63] L. J. Jiang, Y. S. Zhou, W. Xiong, et al., "Two-photon polymerization: investigation of chemical and mechanical properties of resins using Raman microspectroscopy," *Opt. Lett.*, vol. 39, no. 10, p. 3034, 2014.

[64] A. Žukauskas, I. Matuliene, D. Paipulas, G. Niaura, M. Malinauskas, and R. Gadonas, "Tuning the refractive index in 3D direct laser writing lithography: towards GRIN microoptics," *Laser Photonics Rev.*, vol. 9, no. 6, pp. 706–712, 2015.

[65] J. Wu, Z. Zhao, C. M. Hamel, et al., "Evolution of material properties during free radical photopolymerization," *J. Mech. Phys. Solid.*, vol. 112, pp. 25–49, 2018.

[66] B. Steyrer, B. Busetti, G. Harakály, R. Liska, and J. Stampfl, "Hot Lithography vs. room temperature DLP 3D-printing of a dimethacrylate," *Addit. Manuf.*, vol. 21, pp. 209–214, 2018.

[67] L. Jiang, W. Xiong, Y. Zhou, et al., "Performance comparison of acrylic and thiol-acrylic resins in two-photon polymerization," *Opt. Express*, vol. 24, no. 12, p. 13687, 2016.

[68] C. Decker, "Kinetic study and new applications of UV radiation curing," *Macromol. Rapid Commun.*, vol. 23, no. 18, pp. 1067–1093, 2002.

[69] O. Konuray, X. Fernández-Francos, X. Ramis, and À. Serra, "State of the art in dual-curing acrylate systems," *Polymers*, vol. 10, p. 178, 2018.

[70] F. Gamardella, V. Sabatini, X. Ramis, and À. Serra, "Tailor-made thermosets obtained by sequential dual-curing combining isocyanate-thiol and epoxy-thiol click reactions," *Polymer*, vol. 174, pp. 200–209, 2019.

[71] D. Guzmán, X. Ramis, X. Fernández-Francos, S. De la Flor, and A. Serra, "New bio-based materials obtained by thiol-ene/thiol-epoxy dual curing click procedures from eugenol derivates," *Eur. Polym. J.*, vol. 93, pp. 530–544, 2017.

[72] E. Waller and G. von Freymann, "Spatio-temporal proximity characteristics in 3D μ-printing via multi-photon absorption," *Polymers*, vol. 8, no. 8, pp. 1–13, 2016.

[73] M. Y. Zakharina, V. B. Fedoseev, Y. V. Chechet, S. A. Chesnokov, and A. S. Shaplov, "Effect of viscosity of dimethacrylate ester-based compositions on the kinetics of their photopolymerization in presence of o-quinone photoinitiators," *Polym. Sci. Ser. B*, vol. 59, pp. 665–673, 2017.

[74] P. Kardar, M. Ebrahimi, and S. Bastani, "Influence of temperature and light intensity on the photocuring process and kinetics parameters of a pigmented UV curable system," *J. Therm. Anal. Calorim.*, vol. 118, no. 1, pp. 541–549, 2014.

[75] M. G. Hennessy, A. Vitale, J. T. Cabral, and O. K. Matar, "Role of heat generation and thermal diffusion during frontal photopolymerization," *Phys. Rev. E*, vol. 92, no. 2, p. 022403, 2015.

[76] A. Vitale and J. Cabral, "Frontal conversion and uniformity in 3D printing by photopolymerisation," *Materials*, vol. 9, no. 9, p. 760, 2016.

[77] K. Takada, K. Kaneko, Y.-D. Li, S. Kawata, Q.-D. Chen, and H.-B. Sun, "Temperature effects on pinpoint photopolymerization and polymerized micronanostructures," *Appl. Phys. Lett.*, vol. 92, no. 4, p. 041902, 2008.

[78] X.-Z. Dong, Z.-S. Zhao, and X.-M. Duan, "Improving spatial resolution and reducing aspect ratio in multiphoton polymerization nanofabrication," *Appl. Phys. Lett.*, vol. 92, p. 091113, 2008.

[79] M. Malinauskas, H. Gilbergs, A. Žukauskas, V. Purlys, D. Paipulas, and R. Gadonas, "A femtosecond laser-induced two-photon photopolymerization technique for structuring microlenses," *J. Opt.*, vol. 12, p. 3, 2010.

[80] T. Tičkūnas, D. Paipulas, and V. Purlys, "Dynamic voxel size tuning for direct laser writing," *Opt. Mater. Express*, vol. 10, no. 6, pp. 1432–1439, 2020.

[81] F. Burmeister, S. Steenhusen, R. Houbertz, U. D. Zeitner, S. Nolte, and A. Tünnermann, "Materials and technologies for fabrication of three-dimensional microstructures with sub-100 nm feature sizes by two-photon polymerization," *J. Laser Appl.*, vol. 24, no. 4, pp. 042014–849, 2012.

[82] V. F. Paz, M. Emons, K. Obata, et al., "Development of functional sub-100 nm structures with 3D two-photon polymerization technique and optical methods for characterization," *J. Laser Appl.*, vol. 24, p. 4042004, 2012.

[83] W. Haske, V. W. Chen, J. M. Hales, et al., "65 nm feature sizes using visible wavelength 3-D multiphoton lithography," *Opt. Express*, vol. 15, pp. 3426–3436, 2007.

[84] S. Juodkazis, V. Mizeikis, K. K. Seet, M. Miwa, and H. Misawa, "Two-photon lithography of nanorods in SU-8 photoresist," *Nanotechnology*, vol. 16, p. 6, 2005.

[85] D. Tan, Y. Li, F. Qi, et al., "Reduction in feature size of two-photon polymerization using SCR500," *Appl. Phys. Lett.*, vol. 90, no. 7, pp. 071106–4, 2007.

[86] N. Uppal and P. S. Shiakolas, "Process sensitivity analysis and resolution prediction for the two photon polymerization of micro/nano structures," *J. Manuf. Sci. Eng.*, vol. 131, no. 5, pp. 0510181–0510189, 2009.

[87] S. Polyakov, F. Yoshino, and G. Stegeman, "Interplay between self-focusing and high-order multiphoton absorption," *J. Opt. Soc. Am. B*, vol. 18, no. 12, p. 1891, 2001.

[88] A. Dubietis, E. Gaižauskas, G. Tamošauskas, and P. Di Trapani, "Light filaments without self-channeling," *Phys. Rev. Lett.*, vol. 92, no. 25, pp. 1–4, 2004.

[89] H. Cheng, C. Xia, M. Zhang, S. M. Kuebler, and X. Yu, "Fabrication of high-aspect-ratio structures using Bessel-beam-activated photopolymerization," *Appl. Opt.*, vol. 58, no. 13, pp. D91–D97, 2019.

[90] E. G. Gamaly, *Femtosecond Laser-matter Interactions: Theory, Experiments, and Applications*, Singapore, Pan Stanford Publishing, 2011.

[91] S. Juodkazis, V. Mizeikis, S. Matsuo, K. Ueno, and H. Misawa, "Three-dimensional micro- and nano-structuring of materials by tightly focused laser radiation," *Bull. Chem. Soc. Jpn.*, vol. 81, no. 4, pp. 411–448, 2008.

[92] C. Kerse, H. Kalaycıoğlu, P. Elahi, et al., "Ablation-cooled material removal with ultrafast bursts of pulses," *Nature*, vol. 7618, no. 537, pp. 84–88, 2016.

[93] D. W. Beauerle, *Laser Processing and Chemistry*, 4th ed., Heidelberg, Springer-Verlag Berlin Heidelberg, 2011, p. 851.

[94] J. B. Mueller, J. Fischer, Y. J. Mange, T. Nann, and M. Wegener, "In-situ local temperature measurement during three-dimensional direct laser writing," *Appl. Phys. Lett.*, vol. 103, p. 123107, 2013.

[95] N. Uppal and P. S. Shiakolas, "Modeling of temperature-dependent diffusion and polymerization kinetics and their effects on two-photon polymerization dynamics," *J. Micro/ Nanolith. MEMS MOEMS*, vol. 7, no. 4, p. 043002, 2008.

[96] E. Stankevičius, E. Daugnoraite, and G. Račiukaitis, "Photopolymerization differences by using nanosecond and picosecond laser pulses," *Opt. Express*, vol. 25, no. 5, pp. 4819–4830, 2018.

[97] T. Baldacchini, S. Snider, and R. Zadoyan, "Two-photon polymerization with variable repetition rate bursts of femtosecond laser pulses," *Opt. Express*, vol. 20, no. 28, pp. 29890–29899, 2012.

[98] S. Varapnickas, D. Baziulytė-Paulavičienė, S. Šakirzanovas, and M. Malinauskas, "Upconverting nanocrystals as luminescent temperature probes for local-heating imaging during direct laser writing 3D nanolithography," in *Nanophotonics Australasia 2017*, vol. 10456, Melbourne, International Society for Optics and Photonics, 2018, p. 104564F.

[99] T. P. Onanuga, *Process Modeling of Two-photon and Grayscale Laser Direct-Write Lithography*, PhD thesis, Erlangen, Friedrich-Alexander-Universität Erlangen- Nürnber, 2019, p. 142.

[100] A. Lasagni, D. Yuan, P. Shao, and S. Das, "Fabrication of periodic microstructures in pentaerythritol triacrylate through femtosecond laser interference two-photon polymerization," *Adv. Eng. Mater.*, vol. 11, no. 7, pp. 595–599, 2009.

[101] B. Tan, K. Venkatakrishnan, and A. Makaronets, "Effects of pulsewidth on two-photon polymerization," *Des. Monomers Polym.*, vol. 16, no. 2, pp. 145–150, 2013.

[102] L. Jonušauskas, D. Gailevičius, S. Rekštytė, T. Baldacchini, S. Juodkazis, and M. Malinauskas, "Mesoscale laser 3D printing," *Opt. Express*, vol. 27, no. 11, pp. 15205–15221, 2019.

[103] S. Maruo, T. Hasegawa, and N. Yoshimura, "Single-anchor support and supercritical CO_2 drying enable high-precision microfabrication of three-dimensional structures," *Opt. Express*, vol. 17, no. 23, p. 20945, 2009.

[104] A. Ovsianikov, X. Shizhou, M. Farsari, M. Vamvakaki, C. Fotakis, and B. N. Chichkov, "Shrinkage of microstructures produced by two-photon polymerization of Zr-based hybrid photosensitive materials," *Opt. Express*, vol. 17, no. 4, p. 2143, 2009.

[105] D. Gailevičius, S. Sakirzanovas, V. Padolskyte, et al., "Fabrication of 3D glass-ceramic micro-/nano-structures by direct laser writing lithography and pyrolysis," in *Advanced Fabrication Technologies for Micro/Nano Optics and Photonics XI*, vol. 10544, San Francisco, International Society for Optics and Photonics, 2018, p. 1054416.

[106] J. S. Oakdale, J. Ye, W. L. Smith, and J. Biener, "Post-print UV curing method for improving the mechanical properties of prototypes derived from two-photon lithography," *Opt. Express*, vol. 24, no. 24, p. 27077, 2016.

[107] N. Tsutsumi, N. Sakamoto, R. Nakamura, K. Kinashi, and W. Sakai, "Influence of baking conditions on 3D microstructures by direct laser writing in negative photoresist SU-8 via two-photon polymerization," *J. Laser Appl.*, vol. 29, p. 042010, 2017.

[108] G. Seniutinas, A. Balčytis, I. Reklaitis, et al., "Tipping solutions: emerging 3D nano-fabrication/-imaging technologies," *Nanophotonics*, vol. 6, no. 5, pp. 923–941, 2017.

[109] J. Fischer, G. Von Freymann, and M. Wegener, "The materials challenge in diffraction-unlimited direct-laser-writing optical lithography," *Adv. Mater.*, vol. 22, no. 32, pp. 3578–3582, 2010.

[110] R. Wollhofen, J. Katzmann, C. Hrelescu, J. Jacak, and T. A. Klar, "120 nm resolution and 55 nm structure size in STED-lithography," *Opt. Express*, vol. 21, no. 9, pp. 10831–10840, 2013.

[111] N. Li, R. R. Gattass, E. Gershgoren, H. Hwang, and J. T. Fourkas, "Achieving/20 resolution by one-color initiation and

[112] N. Liaros and J. T. Fourkas, "Ten years of two-color photolithography [Invited]," *Opt. Mater. Express*, vol. 9, no. 7, pp. 3006–3020, 2019.

[113] T. F. Scott, B. A. Kowalski, A. C. Sullivan, Ch. N. Bowman, and R. R. McLeod, "Two-color single-photon photoinitiation and photoinhibition for subdiffraction photolithography," *Science*, vol. 324, no. 5929, pp. 913–917, 2009.

[114] I. Sakellari, E. Kabouraki, D. Gray, et al., "Diffusion-Assisted high-resolution direct femtosecond laser writing," *ACS Nano*, vol. 6, no. 3, pp. 2302–2311, 2012.

[115] Y. Gan, Z. Cao, R. A. Evans, and M. Gu, "Three-dimensional deep sub-diffraction optical beam lithography with 9 nm feature size," *Nat. Commun.*, vol. 4, no. 1, pp. 1–7, 2013.

[116] Z. Gan, M. D. Turner, and M. Gu, "Biomimetic gyroid nanostructures exceeding their natural origins," *Sci. Adv.*, vol. 2, no. 5, p. e1600084, 2016.

[117] R. Grunwald and M. Bock, "Needle beams: A review," *Adv. Phys. X*, vol. 5, no. 1, p. 1736950, 2020.

[118] M. Manousidaki, D. G. Papazoglou, M. Farsari, and S. Tzortzakis, "Abruptly autofocusing beams enable advanced multiscale photo-polymerization," *Optica*, vol. 3, p. 525, 2016.

[119] R. J. Winfield, B. Bhuian, S. O'Brien, and G. M. Crean, "Refractive femtosecond laser beam shaping for two-photon polymerization," *Appl. Phys. Lett.*, vol. 90, no. 11, p. 111115, 2007.

[120] B. Bhuian, R. J. Winfield, S. O'Brien, and G. M. Crean, "Pattern generation using axicon lens beam shaping in two-photon polymerisation," *Appl. Surf. Sci.*, vol. 254, no. 4, pp. 841–844, 2007.

[121] M. Manousidaki, D. G. Papazoglou, M. Farsari, and S. Tzortzakis, "Long-scale multiphoton polymerization voxel growth investigation using engineered Bessel beams," *Opt. Mater. Express*, vol. 9, no. 7, p. 2838, 2019.

[122] M. Manousidaki, V. Y. Fedorov, D. G. Papazoglou, M. Farsari, and S. Tzortzakis, "Ring-Airy beams at the wavelength limit," *Opt. Lett.*, vol. 43, no. 5, p. 1063, 2018.

[123] S. Matsuo, S. Juodkazis, and H. Misawa, "Femtosecond laser microfabrication of periodic structures using a microlens array," *Appl. Phys. A*, vol. 80, no. 4, pp. 683–685, 2005.

[124] J. I. Kato, N. Takeyasu, Y. Adachi, H.-B. Sun, and S. Kawata, "Multiple-spot parallel processing for laser micronanofabrication," *Appl. Phys. Lett.*, vol. 86, no. 4, p. 044102, 2005.

[125] V. Hahn, P. Kiefer, T. Frenzel, et al., "Rapid assembly of small materials building blocks (voxels) into large functional 3D metamaterials," *Adv. Funct. Mater.*, vol. 30, p. 1907795, 2020.

[126] C. Maibohm, O. F. Silvestre, J. Borme, M. Sinou, K. Heggarty, and J. B. Nieder, "Multi-beam two-photon polymerization for fast large area 3D periodic structure fabrication for bioapplications," *Sci. Rep.*, vol. 10, no. 1, p. 8740, 2020.

[127] B. Xu, W. Hu, W. Du, et al., "Arch-like microsorters with multi-modal and clogging-improved filtering functions by using femtosecond laser multifocal parallel microfabrication," *Opt. Express*, vol. 25, no. 14, p. 16739, 2017.

[128] K. Obata, J. Koch, U. Hinze, and B. N. Chichkov, "Multi-focus two-photon polymerization technique based on individually

deactivation of polymerization," *Science*, vol. 324, no. 5929, pp. 910–913, 2009.

controlled phase modulation," *Opt. Express*, vol. 18, no. 16, p. 17193, 2010.

[129] Q. Geng, D. Wang, P. Chen, and S. C. Chen, "Ultrafast multi-focus 3-D nano-fabrication based on two-photon polymerization," *Nat. Commun.*, vol. 10, no. 1, pp. 1–7, 2019.

[130] T. Zandrini, O. Shan, V. Parodi, G. Cerullo, M. T. Raimondi, and R. Osellame, "Multi-foci laser microfabrication of 3D polymeric scaffolds for stem cell expansion in regenerative medicine," *Sci. Rep.*, vol. 9, no. 1, p. 11761, 2019.

[131] M. Manousidaki, D. G. Papazoglou, M. Farsari, and S. Tzortzakis, "3D holographic light shaping for advanced multiphoton polymerization," *Opt. Lett.*, vol. 45, no. 1, p. 85, 2020.

[132] G. Vizsnyiczai, L. Kelemen, and P. Ormos, "Holographic multi-focus 3D two-photon polymerization with real-time calculated holograms," *Opt. Express*, vol. 22, no. 20, p. 24217, 2014.

[133] C. Zhang, Y. Hu, J. Li, et al., "An improved multi-exposure approach for high quality holographic femtosecond laser patterning," *Appl. Phys. Lett.*, vol. 105, p. 22, 2014.

[134] D. Yang, L. Liu, Q. Gong, and Y. Li, "Rapid two-photon polymerization of an arbitrary 3D microstructure with 3D focal field engineering," *Macromol. Rapid Commun.*, vol. 40, no. 8, p. 1900041, 2019.

[135] B. E. Kelly, I. Bhattacharya, H. Heidari, M. Shusteff, C. M. Spadaccini, and H. K. Taylor, "Volumetric additive manufacturing via tomographic reconstruction," *Science*, vol. 363, no. 6431, pp. 1075–1079, 2019.

[136] W. Lin, D. Chen, and S.-C. Chen, "Emerging micro-additive manufacturing technologies enabled by novel optical methods," *Photonics Res.*, vol. 8, no. 12, pp. 1827–1842, 2020.

[137] W. H. Teh, U. Dürig, G. Salis, et al., "SU-8 for real three-dimensional subdiffraction-limit two-photon microfabrication," *Appl. Phys. Lett.*, vol. 84, no. 20, pp. 4095–4097, 2004.

[138] M. Farsari and B. N. Chichkov, "Two-photon fabrication," *Nat. Photonics*, vol. 3, no. 8, pp. 450–452, 2009.

[139] M. Farsari, M. Vamvakaki, and B. N. Chichkov, "Multiphoton polymerization of hybrid materials," *J. Opt.*, vol. 12, no. 12, p. 124001, 2010.

[140] W. Zhou, et al., "An efficient two-photon-generated photoacid applied to positive-tone 3D microfabrication," *Science*, vol. 296, no. 5570, pp. 1106–1109, 2002.

[141] S. Maruo and S. Kawata, "Two-photon-absorbed near-infrared photopolymerization for three-dimensional microfabrication," *J. Microelectromech. Syst.*, vol. 7, no. 4, pp. 411–415, 1998.

[142] T. Gissibl, S. Thiele, A. Herkommer, and H. Giessen, "Two-photon direct laser writing of ultracompact multi-lens objectives," *Nat. Photonics*, vol. 10, no. 8, pp. 554–560, 2016.

[143] K. Weber, Z. Wang, S. Thiele, A. Herkommer, and H. Giessen, "Distortion-free multi-element Hypergon wide-angle micro-objective obtained by femtosecond 3D printing," *Opt. Lett.*, vol. 45, no. 10, p. 2784, 2020.

[144] S. Thiele, C. Pruss, A. M. Herkommer, and H. Giessen, "3D printed stacked diffractive microlenses," *Opt. Express*, vol. 27, no. 24, p. 35621, 2019.

[145] H. Wang, Y. Liu, Q. Ruan, et al., "Off-Axis holography with uniform illumination via 3D printed diffractive optical elements," *Adv. Opt. Mater.*, vol. 7, no. 12, p. 1900068, 2019.

[146] J. Lölsberg, J. Linkhorst, A. Cinar, A. Jans, A. J. C. Kuehne, and M. Wessling, "3D nanofabrication inside rapid prototyped microfluidic channels showcased by wet-spinning of single micrometre fibres," *Lab Chip*, vol. 18, no. 9, pp. 1341–1348, 2018.

[147] T. Y. Huang, M. S. Sakar, A. Mao, et al., "3D printed microtransporters: compound micromachines for spatiotemporally controlled delivery of therapeutic agents," *Adv. Mater.*, vol. 27, no. 42, pp. 6644–6650, 2015.

[148] J. Jang, J. y. Kim, Y. C. Kim, et al., "A 3D microscaffold cochlear electrode array for steroid elution," *Adv. Healthcare Mater.*, vol. 8, no. 20, p. 1900379, 2019.

[149] K. K. Seet, S. Juodkazis, V. Jarutis, and H. Misawa, "Feature-size reduction of photopolymerized structures by femtosecond optical curing of SU-8," *Appl. Phys. Lett.*, vol. 89, p. 024106, 2006.

[150] J. Li, X. Li, T. Luo, et al., "Development of a magnetic microrobot for carrying and delivering targeted cells," *Sci. Rob.*, vol. 3, no. 19, pp. 1–12, 2018.

[151] D. Wu, Q.-D. Chen, L.-G. Niu, et al., "Femtosecond laser rapid prototyping of nanoshells and suspending components towards microfluidic devices," *Lab Chip*, vol. 9, no. 16, pp. 2391–2394, 2009.

[152] S. Jariwala, B. Tan, and K. Venkatakrishnan, "Micro-fluidic channel fabrication via two-photon absorption (TPA) polymerization assisted ablation," *J. Micromech. Microeng.*, vol. 19, no. 11, p. 115023, 2009.

[153] G. Kumi, C. O. Yanez, K. D. Belfield, and J. T. Fourkas, "High-speed multiphoton absorption polymerization: fabrication of microfluidic channels with arbitrary cross-sections and high aspect ratios," *Lab Chip*, vol. 10, no. 8, pp. 1057–1060, 2010.

[154] H. Lorenz, M. Despont, N. Fahrni, N. LaBianca, P. Renaud, and P. Vettiger, "SU-8: A low-cost negative resist for MEMS," *J. Micromech. Microeng.*, vol. 7, no. 3, pp. 121–124, 1997.

[155] J. Kopeček, "Hydrogel biomaterials: A smart future?," *Biomaterials*, vol. 28, no. 34, pp. 5185–5192, 2007.

[156] S. R. Caliari and J. A. Burdick, "A practical guide to hydrogels for cell culture," *Nat. Methods*, vol. 13, no. 5, pp. 405–414, 2016.

[157] K. Arcaute, B. Mann, and R. Wicker, "Stereolithography of spatially controlled multi-material bioactive poly(ethylene glycol) scaffolds," *Acta Biomater.*, vol. 6, no. 3, pp. 1047–1054, 2010.

[158] T. M. Seck, F. P. W. Melchels, J. Feijen, and D. W. Grijpma, "Designed biodegradable hydrogel structures prepared by stereolithography using poly(ethylene glycol)/poly (d,l -lactide)-based resins," *J. Contr. Release*, vol. 148, no. 1, pp. 34–41, 2010.

[159] F. Klein, B. Richter, T. Striebel, et al., "Two-component polymer scaffolds for controlled three-dimensional cell culture," *Adv. Mater.*, vol. 23, no. 11, pp. 1341–1345, 2011.

[160] S. H. Lee, J. J. Moon, and J. L. West, "Three-dimensional micropatterning of bioactive hydrogels via two-photon laser scanning photolithography for guided 3D cell migration," *Biomaterials*, vol. 29, no. 20, pp. 2962–2968, 2008.

[161] A. Ovsianikov, M. Gruene, M. Pflaum, et al., "Laser printing of cells into 3D scaffolds," *Biofabrication*, vol. 2, no. 1, p. 014104, 2010.

[162] E. Yang, S. Miao, J. Zhong, Z. Zhang, D. K. Mills, and L. G. Zhang, "Bio-based polymers for 3D printing of bioscaffolds," *Polym. Rev.*, vol. 58, no. 4, pp. 668–687, 2018.

[163] E. Skliutas, S. Kasetaite, L. Jonušauskas, J. Ostrauskaite, and M. Malinauskas, "Photosensitive naturally derived resins toward optical 3-D printing," *Opt. Eng.*, vol. 57, no. 4, p. 1, 2018.

[164] K. Na, S. Shin, H. Lee, et al., "Effect of solution viscosity on retardation of cell sedimentation in DLP 3D printing of gelatin methacrylate/silk fibroin bioink," *J. Ind. Eng. Chem.*, vol. 61, pp. 340–347, 2018.

[165] W. Ye, H. Li, K. Yu, et al., "3D printing of gelatin methacrylate-based nerve guidance conduits with multiple channels," *Mater. Des.*, vol. 192, p. 108757, 2020.

[166] J. Guit, M. B. L. Tavares, J. Hul, et al., "Photopolymer resins with biobased methacrylates based on soybean oil for stereolithography," *ACS Appl. Polym. Mater.*, vol. 2, no. 2, pp. 949–957, 2020.

[167] A. W. Bassett, A. E. Honnig, C. M. Breyta, I. C. Dunn, J. J. La Scala, and J. F. Stanzione, "Vanillin-based resin for additive manufacturing," *ACS Sustain. Chem. Eng.*, vol. 8, no. 14, pp. 5626–5635, 2020.

[168] J. T. Sutton, K. Rajan, D. P. Harper, and S. C. Chmely, "Lignin-containing photoactive resins for 3D printing by stereolithography," *ACS Appl. Mater. Interfaces*, vol. 10, pp. 36456–36463, 2018.

[169] V. S. D. Voet, T. Strating, G. H. M. Schnelting, et al., "Biobased acrylate photocurable resin formulation for stereolithography 3D printing," *ACS Omega*, vol. 3, no. 2, pp. 1403–1408, 2018.

[170] V. S. D. Voet, G. H. M. Schnelting, J. Xu, K. Loos, R. Folkersma, and J. Jager, "Stereolithographic 3D printing with renewable acrylates," *JoVE*, vol. 139, p. e58177, 2018.

[171] A. Champion, X. Allonas, C. Croutxé-Barghorn, A.-S. Schuller, and C. Delaite, "Carbohydrate-derived unsaturated polyester for high bio-based carbon content photopolymer," *Prog. Org. Coating*, vol. 131, pp. 240–246, 2019.

[172] X. Wang, Z. Wei, C. Z. Baysah, M. Zheng, and J. Xing, "Biomaterial-based microstructures fabricated by two-photon polymerization microfabrication technology," *RSC Adv.*, vol. 9, no. 59, pp. 34472–34480, 2019.

[173] S. Schoch, P. E. Castillo, T. Jo, et al., "RIM1α forms a protein scaffold for regulating neurotransmitter release at the active zone," *Nature*, vol. 415, no. 6869, pp. 321–326, 2002.

[174] B. Kaehr and J. B. Shear, "Multiphoton fabrication of chemically responsive protein hydrogels for microactuation," *Proc. Natl. Acad. Sci. U.S.A.*, vol. 105, no. 26, pp. 8850–8854, 2008.

[175] A. Ovsianikov, A. Deiwick, S. Van Vlierberghe, et al., "Laser fabrication of three-Dimensional CAD scaffolds from photosensitive gelatin for applications in tissue engineering," *Biomacromolecules*, vol. 12, no. 4, pp. 851–858, 2011.

[176] M. Gebinoga, J. Katzmann, U. Fernekorn, et al., "Multi-photon structuring of native polymers: A case study for structuring natural proteins," *Eng. Life Sci.*, vol. 13, no. 4, pp. 368–375, 2013.

[177] A. Koroleva, S. Gittard, S. Schlie, A. Deiwick, S. Jockenhoevel, and B. Chichkov, "Fabrication of fibrin scaffolds with controlled microscale architecture by a two-photon polymerization-micromolding technique," *Biofabrication*, vol. 4, no. 1, p. 015001, 2012.

[178] K. Parkatzidis, M. Chatzinikolaidou, M. Kaliva, A. Bakopoulou, M. Farsari, and M. Vamvakaki, "Multiphoton 3D printing of biopolymer-based hydrogels," *ACS Biomater. Sci. Eng.*, vol. 5, no. 11, pp. 6161–6170, 2019.

[179] K. Parkatzidis, M. Chatzinikolaidou, E. Koufakis, M. Kaliva, M. Farsari, and M. Vamvakaki, "Multi-photon polymerization of bio-inspired, thymol-functionalized hybrid materials with biocompatible and antimicrobial activity," *Polym. Chem.*, vol. 11, p. 4078, 2020.

[180] M. Rothammer, M.-C. Heep, G. von Freymann, and C. Zollfrank, "Enabling direct laser writing of cellulose-based submicron architectures," *Cellulose*, vol. 25, no. 10, pp. 6031–6039, 2018.

[181] Y. L. Sun, Q. Li, S.-M. Sun, et al., "Aqueous multiphoton lithography with multifunctional silk-centred bio-resists," *Nat. Commun.*, vol. 6, no. 1, pp. 1–10, 2015.

[182] K. Liu, J. Jiang, and T. H. Tao, "Fabrication of 3D silk microstructures by direct two-photon polymerization," in *Proceedings of the IEEE International Conference on Micro Electro Mechanical Systems (MEMS)*, vol. 2019-January, Seoul, Institute of Electrical and Electronics Engineers Inc., 2019, pp. 522–524.

[183] O. Kufelt, A. El-Tamer, C. Sehring, S. Schlie-Wolter, and B. N. Chichkov, "Hyaluronic acid based materials for scaffolding via two-photon polymerization," *Biomacromolecules*, vol. 15, no. 2, pp. 650–659, 2014.

[184] A. Berg, R. Wyrwa, J. Weisser, et al., "Synthesis of photopolymerizable hydrophilic macromers and evaluation of their applicability as reactive resin components for the fabrication of three-dimensionally structured hydrogel matrices by 2-photon-polymerization," *Adv. Eng. Mater.*, vol. 13, no. 9, pp. B274–B284, 2011.

[185] K. H. Haas and H. Wolter, "Synthesis, properties and applications of inorganic-organic copolymers (ORMOCER®s)," *Curr. Opin. Solid State Mater. Sci.*, vol. 4, no. 6, pp. 571–580, 1999.

[186] T. M. Hsieh, C. W. Benjamin Ng, K. Narayanan, A. C. A. Wan, and J. Y. Ying, "Three-dimensional microstructured tissue scaffolds fabricated by two-photon laser scanning photolithography," *Biomaterials*, vol. 31, no. 30, pp. 7648–7652, 2010.

[187] J. Serbin, A. Egbert, A. Ostendorf, et al., "Femtosecond laser-induced two-photon polymerization of inorganic-organic hybrid materials for applications in photonics," *Opt. Lett.*, vol. 28, no. 5, pp. 301–303, 2003.

[188] S. Rekštytė, D. Paipulas, M. Malinauskas, and V. Mizeikis, "Microactuation and sensing using reversible deformations of laser-written polymeric structures," *Nanotechnology*, vol. 28, no. 12, p. 12, 2017.

[189] A. Ovsianikov, S. Schlie, A. Ngezahayo, A. Haverich, and B. N. Chichkov, "Two-photon polymerization technique for microfabrication of CAD-designed 3D scaffolds from commercially available photosensitive materials," *J. Tissue Eng. Regen. Med.*, vol. 1, no. 6, pp. 443–449, 2007.

[190] H. Jeon, H. Hidai, D. J. Hwang, and C. P. Grigoropoulos, "Fabrication of arbitrary polymer patterns for cell study by two-photon polymerization process," *J. Biomed. Mater. Res.*, vol. 93A, no. 1, pp. 56–66, 2009.

[191] P. Danilevicius, S. Rekštytė, R. Gadonas, et al., "Micro-structured polymer scaffolds fabricated by direct laser writing for tissue engineering," *J. Biomed. Opt.*, vol. 17, no. 8, p. 081405, 2012.

[192] K. H. Haas, S. Amberg-Schwab, and K. Rose, "Functionalized coating materials based on inorganic-organic polymers," *Thin Solid Films*, vol. 351, nos 1-2, pp. 198–203, 1999.

[193] A. Marino, G. Ciofani, C. Filippeschi, et al., "Two-photon polymerization of sub-micrometric patterned surfaces: investigation of cell-substrate interactions and improved differentiation of neuron-like cells," *ACS Appl. Mater. Interfaces*, vol. 5, no. 24, pp. 13012–13021, 2013.

[194] A. C. Scheiwe, S. C. Frank, T. J. Autenrieth, M. Bastmeyer, and M. Wegener, "Subcellular stretch-induced cytoskeletal response of single fibroblasts within 3D designer scaffolds," *Biomaterials*, vol. 44, pp. 186–194, 2015.

[195] A. Ovsianikov, A. Ostendorf, and B. N. Chichkov, "Three-dimensional photofabrication with femtosecond lasers for applications in photonics and biomedicine," *Appl. Surf. Sci.*, vol. 253, no. 15, pp. 6599–6602, 2007.

[196] S. Jariwala, K. Venkatakrishnan, and B. Tan, "Single step self-enclosed fluidic channels via two photon absorption (TPA) polymerization," *Opt. Express*, vol. 18, no. 2, p. 1630, 2010.

[197] A. Marino, A. Desii, M. Pellegrino, et al., "Nanostructured Brownian surfaces prepared through two-photon polymerization: investigation of stem cell response," *ACS Nano*, vol. 8, no. 11, pp. 11869–11882, 2014.

[198] L. Jonušauskas, D. Gailevičius, L. Mikoliūnaitė, et al., "Optically clear and resilient free-form μ-optics 3D-printed via ultrafast laser lithography," *Materials*, vol. 10, no. 1, 2017, https://doi.org/10.3390/ma10010012.

[199] M. Malinauskas, A. Žukauskas, V. Purlys, et al., "Femtosecond laser polymerization of hybrid/integrated microoptical elements and their characterization," *J. Opt.*, vol. 12, p. 12, 2010.

[200] Q. Sun, S. Juodkazis, N. Murazawa, V. Mizeikis, and H. Misawa, "Freestanding and movable photonic microstructures fabricated by photopolymerization with femtosecond laser pulses," *J. Micromech. Microeng.*, vol. 20, no. 3, p. 035004, 2010.

[201] Y. Tian, H. Kwon, Y. C. Shin, and G. B. King, "Fabrication and characterization of photonic crystals in photopolymer SZ2080 by two-photon polymerization using a femtosecond laser," *J. Micro Nano-Manuf.*, vol. 2, p. 3, 2014.

[202] C. Schizas, V. Melissinaki, A. Gaidukeviciute, et al., "On the design and fabrication by two-photon polymerization of a readily assembled micro-valve," *Int. J. Adv. Manuf. Technol.*, vol. 48, nos 5-8, pp. 435–441, 2009.

[203] P. S. Timashev, M. V. Vedunova, D. Guseva, et al., "3D in vitro platform produced by two-photon polymerization for the analysis of neural network formation and function," *Biomed. Phys. Eng. Express*, vol. 2, no. 3, p. 035001, 2016.

[204] J. Mačiulaitis, M. Deveikytė, S. Rekštytė, et al., "Preclinical study of SZ2080 material 3D microstructured scaffolds for cartilage tissue engineering made by femtosecond direct laser writing lithography," *Biofabrication*, vol. 7, p. 1, 2015.

[205] G. Flamourakis, I. Spanos, Z. Vangelatos, et al., "Laser-made 3D auxetic metamaterial scaffolds for tissue engineering applications," *Macromol. Mater. Eng.*, vol. 305, p. 2000238, 2020.

[206] Z. Vangelatos, K. Komvopoulos, J. Spanos, M. Farsari, and C. Grigoropoulos, "Anisotropic and curved lattice members enhance the structural integrity and mechanical performance of architected metamaterials," *Int. J. Solid Struct.*, vol. 193-194, pp. 287–301, 2020.

[207] G. Kenanakis, A. Xomalis, A. Selimis, et al., "Three-dimensional infrared metamaterial with asymmetric transmission," *ACS Photonics*, vol. 2, p. 287, 2015.

[208] D. Gailevičius, L. Jonušauskas, D. Sakalauskas, et al., "Laser nanolithography and pyrolysis of SZ2080 hybrid for slowing light in 3D photonic crystals," in *Advanced Fabrication Technologies for Micro/Nano Optics and Photonics X*, vol. 10115, G. von Freymann, W. V. Schoenfeld, and R. C. Rumpf, Eds, San Francisco, SPIE, 2017, p. 1011511.

[209] I. Sakellari, A. Gaidukeviciute, A. Giakoumaki, et al., "Two-photon polymerization of titanium-containing sol-gel composites for three-dimensional structure fabrication," *Appl. Phys. A*, vol. 100, no. 2, pp. 359–364, 2010.

[210] E. Kabouraki, A. N. Giakoumaki, P. Danilevicius, D. Gray, M. Vamvakaki, and M. Farsari, "Redox multiphoton polymerization for 3D nanofabrication," *Nano Lett.*, vol. 13, no. 8, pp. 3831–3835, 2013.

[211] M. Malinauskas, A. Gaidukevičiūtė, V. Purlys, et al., "Direct laser writing of microoptical structures using a Ge-containing hybrid material," *Metamaterials*, vol. 5, no. 5, pp. 135–140, 2011.

[212] T. S. Drakakis, G. Papadakis, K. Sambani, et al., "Construction of three-dimensional biomolecule structures employing femtosecond lasers," *Appl. Phys. Lett.*, vol. 89, no. 14, p. 144108, 2006.

[213] C. R. Mendonca, D. S. Correa, F. Marlow, T. Voss, P. Tayalia, and E. Mazur, "Three-dimensional fabrication of optically active microstructures containing an electroluminescent polymer," *Appl. Phys. Lett.*, vol. 95, no. 11, p. 113309, 2009.

[214] A. J. G. Otuka, V. Tribuzi, D. S. Corrêa, and C. R. Mendonça, "Emission features of microstructures fabricated by two-photon polymerization containing three organic dyes," *Opt. Mater. Express*, vol. 2, no. 12, p. 1803, 2012.

[215] A. Žukauskas, M. Malinauskas, L. Kontenis, et al., "Organic dye doped microstructures for optically active functional devices fabricated via two-photon polymerization technique," *Lith. J. Phys.*, vol. 50, p. 1, 2010.

[216] M. Farsari, A. Ovsianikov, M. Vamvakaki, et al., "Fabrication of three-dimensional photonic crystal structures containing an active nonlinear optical chromophore," *Appl. Phys. A*, vol. 93, no. 1, pp. 11–15, 2008.

[217] Z. B. Sun, X.-Z. Dong, W.-Q. Chen, S. Nakanishi, X.-M. Duan, and S. Kawata, "Multicolor polymer nanocomposites: in situ synthesis and fabrication of 3D microstructures," *Adv. Mater.*, vol. 20, no. 5, pp. 914–919, 2008.

[218] R. Krini, C. W. Ha, P. Prabhakaran, et al., "Photosensitive functionalized surface-modified quantum dots for polymeric structures via two-photon-initiated polymerization technique," *Macromol. Rapid Commun.*, vol. 36, no. 11, pp. 1108–1114, 2015.

[219] I. Sakellari, E. Kabouraki, D. Karanikolopoulos, et al., "Quantum dot based 3D printed woodpile photonic crystals tuned for the visible," *Nanoscale Adv.*, vol. 1, no. 9, pp. 3413–3423, 2019.

[220] V. W. Chen, N. Sobeshchuk, C. Lafargue, et al., "Three-dimensional organic microlasers with low lasing thresholds fabricated by multiphoton and UV lithography," *Opt. Express*, vol. 22, no. 10, p. 12316, 2014.

[221] K. Kurselis, R. Kiyan, V. N. Bagratashvili, V. K. Popov, and B. N. Chichkov, "3D fabrication of all-polymer conductive microstructures by two photon polymerization," *Opt. Express*, vol. 21, no. 25, 2013, https://doi.org/10.1364/oe.21.031029.31029.

[222] J. M. P. Almeida, V. Tribuzi, R. D. Fonseca, et al., "Femtosecond laser processing of glassy and polymeric matrices containing metals and semiconductor nanostructures," *Opt. Mater.*, vol. 35, no. 12, pp. 2643–2648, 2013.

[223] R. D. Fonseca, D. S. Correa, E. C. Paris, et al., "Fabrication of zinc oxide nanowires/polymer composites by two-photon polymerization," *J. Polym. Sci, Part B: Polym. Phys.*, vol. 52, no. 4, pp. 333–337, 2014.

[224] J. Wang, H. Xia, B.-B. Xu, et al., "Remote manipulation of micronanomachines containing magnetic nanoparticles," *Opt. Lett.*, vol. 34, no. 5, p. 581, 2009.

[225] Y. Tian, Lu D., Jiang H., Lin X., "Preparation of a novel ferrofluidic photoresist for two-photon photopolymerization technique," *J. Magn. Magn Mater.*, vol. 324, no. 20, pp. 3291– 3294, 2012.

[226] X. Xiong, Z.-H. Xue, C. Meng, et al., "Polarization-dependent perfect absorbers/reflectors based on a three-dimensional metamaterial," *Phys. Rev. B*, vol. 88, no. 11, p. 115105, 2013.

[227] B. L. Aekbote, J. Jacak, G. J. Schütz, et al., "Aminosilane-based functionalization of two-photon polymerized 3D SU-8 microstructures," *Eur. Polym. J.*, vol. 48, no. 10, pp. 1745–1754, 2012.

[228] Y. S. Chen, A. Tal, and S. M. Kuebler, "Route to three-dimensional metallized microstructures using cross-linkable epoxide SU-8," *Chem. Mater.*, vol. 19, no. 16, pp. 3858–3860, 2007.

[229] N. Vasilantonakis, K. Terzaki, I. Sakellari, et al., "Three-dimensional metallic photonic crystals with optical bandgaps," *Adv. Mater.*, vol. 24, no. 8, pp. 1101–1105, 2012.

[230] C. N. LaFratta, D. Lim, K. O'Malley, T. Baldacchini, and J. T. Fourkas, "Direct laser patterning of conductive wires on three-dimensional polymeric microstructures," *Chem. Mater.*, vol. 18, no. 8, pp. 2038–2042, 2006.

[231] R. Ameloot, M. B. J. Roeffaers, G. De Cremer, et al., "Metal-organic Framework single crystals as photoactive matrices for the generation of metallic microstructures," *Adv. Mater.*, vol. 23, no. 15, pp. 1788–1791, 2011.

[232] B. Richter, V. Hahn, S. Bertels, et al., "Guiding cell attachment in 3D microscaffolds selectively functionalized with two distinct adhesion proteins," *Adv. Mater.*, vol. 29, no. 5, p. 1604342, 2017.

[233] Y. Jian, Y. He, T. Jiang, C. Li, W. Yang, and J. Nie, "Volume shrinkage of UV-curable coating formulation investigated by real-time laser reflection method," *J. Coating Technol. Res.*, vol. 10, no. 2, pp. 231–237, 2013.

[234] R. J.-Y. Kim, Y.-J. Kim, N.-S. Choi, and I.-B. Lee, "Polymerization shrinkage, modulus, and shrinkage stress related to tooth-restoration interfacial debonding in bulk-fill composites," *J. Dent.*, vol. 43, no. 4, pp. 430–439, 2015.

[235] C. Schmidt and T. Scherzer, "Monitoring of the shrinkage during the photopolymerization of acrylates using hyphenated photorheometry/near-infrared spectroscopy," *J. Polym. Sci, Part B: Polym. Phys.*, vol. 53, no. 10, pp. 729–739, 2015.

[236] B. Lu, P. Xiao, M. Sun, and J. Nie, "Reducing volume shrinkage by low-temperature photopolymerization," *J. Appl. Polym. Sci.*, vol. 104, no. 2, pp. 1126–1130, 2007.

[237] S. Fessel, A. M. Schneider, S. Steenhusen, R. Houbertz, and P. Behrens, "Towards an atomistic model for ORMOCER-I: application of forcefield methods," *J. Sol. Gel Sci. Technol.*, vol. 63, no. 3, pp. 356–365, 2012.

[238] Y. He, M. Yao, and J. Nie, "Shrinkage in UV-curable coatings," in *Protective Coatings: Film Formation and Properties*, Springer International Publishing, 2017, pp. 195–223, https://doi.org/10.1007/978-3-319-51627-1_9.

[239] T. T. Tauböck, A. J. Feilzer, W. Buchalla, C. J. Kleverlaan, I. Krejci, and T. Attin, "Effect of modulated photo-activation on polymerization shrinkage behavior of dental restorative resin composites," *Eur. J. Oral Sci.*, vol. 122, no. 4, pp. 293–302, 2014.

[240] K. A. Berchtold, B. Hacioğlu, J. Nie, N. B. Cramer, J. W. Stansbury, and C. N. Bowman, "Rapid solid-state photopolymerization of cyclic acetal-containing acrylates," *Macromolecules*, vol. 42, no. 7, pp. 2433–2437, 2009.

[241] Q. Shi, B. Sontheimer, N. Nikolay, et al., "Wiring up pre-characterized single-photon emitters by laser lithography," *Sci. Rep.*, vol. 6. no. 1, pp. 1–7, 2016.

[242] S. Rekštytė, T. Jonavičius, and M. Malinauskas, "Direct laser writing of microstructures on optically opaque and reflective surfaces," *Opt. Laser Eng.*, vol. 53, pp. 90–97, 2014.

[243] C. Reinhardt, S. Passinger, B. N. Chichkov, C. Marquart, I. P. Radko, and S. I. Bozhevolnyi, "Laser-fabricated dielectric optical components for surface plasmon polaritons," *Opt. Lett.*, vol. 31, no. 9, pp. 1307–1309, 2006.

[244] D. Wu, L. G. Niu, S. Z. Wu, J. Xu, K. Midorikawa, and K. Sugioka, "Ship-in-a-bottle femtosecond laser integration of optofluidic microlens arrays with center-pass units enabling coupling-free parallel cell counting with a 100% success rate," *Lab Chip*, vol. 15, no. 6, pp. 1515–23, 2015.

[245] S. Thiele, K. Arzenbacher, T. Gissibl, H. Giessen, and A. M. Herkommer, "3D-printed eagle eye: compound microlens system for foveated imaging," *Sci. Adv.*, vol. 3, no. 2, p. e1602655, 2017.

[246] X. Zhou, Y. Hou, and J. Lin, "A review on the processing accuracy of two-photon polymerization," *AIP Adv.*, vol. 5, p. 030701, 2015.

[247] A. C. Uzcategui, A. Muralidharan, V. L. Ferguson, S. J. Bryant, and R. R. McLeod, "Understanding and improving mechanical properties in 3D printed parts using a dual-cure acrylate-based resin for stereolithography," *Adv. Eng. Mater.*, vol. 20, no. 12, p. 1800876, 2018.

[248] E. M. Da Silva, L. T. Poskus, J. G. A. Guimarães, A. d. A. L. Barcellos, and C. E. Fellows, "Influence of light polymerization modes on degree of conversion and crosslink density of dental composites," *J. Mater. Sci. Mater. Med.*, vol. 19, no. 3, pp. 1027–1032, 2008.

[249] J. Purtov, A. Verch, P. Rogin, and R. Hensel, "Improved development procedure to enhance the stability of microstructures created by two-photon polymerization," *Microelectron. Eng.*, vol. 194, pp. 45–50, 2018.

[250] G. Seniutinas, A. Weber, C. Padeste, I. Sakellari, M. Farsari, and C. David, "Beyond 100 nm resolution in 3D laser lithography –

post processing solutions," *Microelectron. Eng.*, vol. 191, pp. 25–31, 2018.

[251] Y. Liu, H. Wang, J. Ho, et al., "Structural color three-dimensional printing by shrinking photonic crystals," *Nat. Commun.*, vol. 10, no. 1, pp. 1–8, 2019.

[252] Z. Vangelatos, L. Wang, and C. P. Grigoropoulos, "Laser pyrolysis for controlled morphing and chemical modification on 3D microlattices," *J. Micromech. Microeng.*, vol. 30, p. 055008, 2020.

[253] Z. Vangelatos, G. X. Gu, and C. P. Grigoropoulos, "Architected metamaterials with tailored 3D buckling mechanisms at the microscale," *Extreme Mech. Lett.*, vol. 33, p. 100580, 2020.

[254] Z. Vangelatos, A. Micheletti, C. P. Grigoropoulos, and F. Fraternali, "Design and testing of bistable lattices with tensegrity architecture and nanoscale features fabricated by multiphoton lithography," *Nanomaterials*, vol. 10, no. 4, p. 652, 2020.

[255] J. Qu, M. Kadic, A. Naber, and M. Wegener, "Micro-structured two-component 3D metamaterials with negative thermal-expansion coefficient from positive constituents," *Sci. Rep.*, vol. 7, no. 1, pp. 1–8, 2017.

[256] G. Flamourakis, I. Spanos, Z. Vangelatos, et al., "Laser-made 3D auxetic metamaterial scaffolds for tissue engineering applications," *Macromol. Mater. Eng.*, vol. 305, no. 7, 2020, https://doi.org/10.1002/mame.202000238.

[257] J. Maciulaitis, S. Rekštytė, M. Bratchikov, et al., "Customization of direct laser lithography-based 3D scaffolds for optimized in vivo outcome," *Appl. Surf. Sci.*, vol. 487, pp. 692–702, 2019.

[258] E. Harnisch, M. Russew, J. Klein, N. König, H. Crailsheim, and R. Schmitt, "Optimization of hybrid polymer materials for 2PP and fabrication of individually designed hybrid microoptical elements thereof," *Opt. Mater. Express*, vol. 5, no. 2, p. 456, 2015.

[259] M. Blaicher, M. R. Billah, J. Kemal, et al., "Hybrid multi-chip assembly of optical communication engines by in situ 3D nano-lithography," *Light Sci. Appl.*, vol. 9, no. 1, pp. 1–11, 2020.

[260] C. R. Ocier, C. A. Corey, D. A. Bacon-Brown, et al., "Direct laser writing of volumetric gradient index lenses and waveguides," *Light Sci. Appl.*, vol. 9, no. 196, p. 14, 2020.

[261] Y. L. Zhang, Y. Tian, H. Wang, et al., "Dual-3D femtosecond laser nanofabrication enables dynamic actuation," *ACS Nano*, vol. 13, no. 4, pp. 4041–4048, 2019.

[262] S. Taniguchi and S. Maruo, "Remotely driven micromachines produced by two- photon microfabrication," in *Three-Dimensional Microfabrication Using Two- Photon Polymerization: Fundamentals, Technology, and Applications*, 2nd ed. T. Baldacchini, Ed., Oxford: William Andrew Publishing, 2020. Chap. Chapter 12 – Remotely Driven Micromachines Produced by Two-Photon Microfabrication, pp. 475–492, https://doi.org/10.1016/B978-0-12-817827-0.00056-4.

[263] P.-I. Dietrich, G. Göring, M. Trappen, et al., "3D-Printed scanning-probe microscopes with integrated optical actuation and read-out," *Small*, vol. 16, no. 2, p. 1904695, 2020.

[264] M. Hunt, M. Taverne, J. Askey, et al., "Harnessing multi-photon absorption to produce three-dimensional magnetic structures at the nanoscale," *Materials*, vol. 13, p. 761, 2020.

[265] Z.-C. Ma, Y.-L. Zhang, B. Han, Q.-D. Chen, and H.-B. Sun, "Femtosecond-laser direct writing of metallic micro/nanostructures: from fabrication strategies to future applications," *Small Methods*, vol. 2, no. 7, p. 1700413, 2018.

[266] C. L. Lay, C. S. L. Koh, Y. H. Lee, et al., "Two-photon-assisted polymerization and reduction: emerging formulations and applications," *ACS Appl. Mater. Interfaces*, vol. 12, pp. 10061–10079, 2020.

[267] S. Maddox, M. Afshar-Mohajer, and M. Zou, "Digitization, replication, and modification of physical surfaces using two-photon lithography," *J. Manuf. Process.*, vol. 54, pp. 180–189, 2020.

[268] J. F. Busche, G. Starke, S. Knickmeier, and A. Dietzel, "Controllable dry adhesion based on two-photon polymerization and replication molding for space debris removal," *Micro Nano Eng.*, vol. 7, p. 100052, 2020.

[269] E. Skliutas, M. Lebedevaite, S. Kasetaite, et al., "A bio-based resin for a multi-scale optical 3D printing," *Sci. Rep.*, vol. 10, p. 9758, 2020.

[270] A. C. Lamont, M. A. Restaino, M. J. Kim, and R. D. Sochol, "A facile multi-material direct laser writing strategy," *Lab Chip*, vol. 19, pp. 2340–2345, 2019.